Supporting Information

Mixed-Valent Ruthenocene–Vinylruthenium Conjugates: Valence Delocalization Despite Chemically Different Redox Sites

Christopher Hassenrück, André Mang, Rainer F. Winter*

University of Konstanz, Department of Chemistry, Universitätsstraße 10, 78457 Konstanz, Germany

Table of Content

1. General Procedures

General Procedures. All syntheses were performed using standard Schlenk techniques under nitrogen atmosphere. The solvents used for synthesis and characterization were dried over appropriate drying agents, distilled and stored under nitrogen atmosphere. The purities of the complexes were determined by NMR spectroscopy and combustion analyses. All chemicals were obtained from commercial suppliers and used without further purification. Details to the synthesis of the required triarylamines and their characterization can be found in the Supporting Information. ^{1}H- and ^{13}C NMR spectra were recorded on a Bruker AVANCE III 400 (B_H = 400 MHz, B_C= 100.6 MHz, B_P = 162 MHz) spectrometer at room temperature. The spectra were referenced to the residual signal of the protonated solvents or, for ^{31}P NMR spectroscopy, to H_3PO_4 as an external standard. Coupling constants are given in Hz.

Cyclic voltammetry was performed in a one compartment cell with 5 to 7 mL of CH_2Cl_2 as the solvent and NBu_4PF_6 (0.1 M) as the supporting electrolyte. A platinum electrode (Ø = 1.1 mm, BASI) was used as the working electrode. It was polished with diamond pastes (1.5 µm and 1 µm particle size) from Buehler&Wirtz. A computer-controlled BASi EPSILON potentiostat was used for recording of the voltammograms. An Ag/AgCl wire pseudo reference electrode and a Pt-wire as auxiliary electrode were used in the measurements. The cell was connected to an argon gas bottle. Potential calibration was performed by adding appropriate quantities of decamethylferrocene (Cp^*_2Fe) after all scans of interest had been acquired. Potentials are reported against the ferrocene/ferrocenium couple, which is 550 mV positive of the $Cp^*_2Fe^{0/+}$ couple under our conditions.

IR and UV/vis/NIR spectroelectrochemistry was performed in a self-built Optically Transparent Thin Layer Electrolysis (OTTLE) cell according to the design of *F. Hartl*.[1] A platinum minigrid as the working and counter electrodes and a thin silver foil as reference electrode are welded in a polyethylene spacer, incorporated into a Teflon housing with electrical connectors and sandwiched in between the CaF_2 plates of a conventional liquid IR cell. 1,2-$C_2H_4Cl_2$ / 0.1 M NBu_4PF_6 was used as the supporting electrolyte. IR/NIR spectra were recorded on a FT-IR Bruker Tensor II instrument. The UV/vis/NIR-measurements were performed on a diode array unit TIDAS by j&m ANALYTIK AG with a spectroscopic window of 250 to 2100 nm. A computer-controlled potentiostat WENKING POS3 was used for controlled electrolysis.

Electron Paramagnetic Resonance (EPR) spectroscopy was performed with an X-Band benchtop spectrometer of the type MINISOPE400MS by Magnettech GmBH. Low-temperature work was conducted by cooling with liquid nitrogen. As thermostat, a temperature controller by the same manufacturer was used. The magnet was cooled using a Thermo Fischer Sci. Inc. HAAKE A10 cooling unit. The complexes were chemically oxidized with appropriate amounts of ferrocenium hexafluorophosphate, in dichloromethane solution at room temperature prior to the measurements. Simulations of the measured spectra was performed using the MATLAB Easyspin program.[2]

Density functional theory (DFT) calculations were performed on the full model complexes using the GAUSSIAN 09 program package.[3] Geometry optimizations were performed without any symmetry constraints. Electronic transitions were calculated by the time-dependent DFT (TD-DFT) method. Within G09 calculations the quasirelativistic effective core pseudopotentials and the corresponding optimized set of basis functions for Ru were used.[4] Polarized double-ζ basis sets (6-31G(d), geometry optimization) were employed together with the pbe1pbe functional.[5] The for the Fe atoms the Wachter basis set implemented in the 6-311G(d) basis sets for transition metals were applied in DFT and TD-DFT calculations.[6] Solvation effects were modeled by the polarizable continuum model (PCM).[7]

2. Synthesis

Ruthenocene[8]

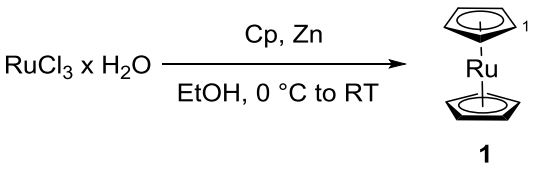

Ruthenium(III) chloride hydrate (17.4 g, 66 mmol, 1 eq) was dissolved in dry ethanol (180 mL). The solution was degassed with nitrogen for 10 min. After cooling to 0 °C, cyclopentadiene (85.6 mL, 68.5 g, 1036 mmol, 15 eq) was added. Zinc dust (45.0 g, 690 mmol, 10 eq) was added in small portions at the same temperature. After complete addition, the suspension was allowed to reach RT and was then stirred for 2 h. The reaction mixture was filtered over a short plug of diatomaceous earth and the filtrate was concentrated under reduced pressure. The residue was dissolved in toluene and filtered over a short column of silica. The solvent was removed under reduced pressure to give fine, slightly yellow crystals in 19 % yield (3.0 g, 13 mmol). **^{1}H-NMR** (400 MHz, $CDCl_3$) δ /ppm = 4.55 (s, 10H, *H*-1).

Formylruthenocene[9]

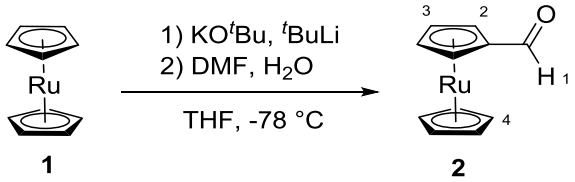

Ruthenocene (**1**) (1.0 g, 4.3 mmol, 1 eq) was dissolved in dry THF (100 mL). Subsequently, 0.5 mL of a 1 M KO^{t}Bu-solution in THF (0.5 mmol, 0.12 eq) were added and the reaction mixture was cooled to -78 °C. At this temperature, ^{t}BuLi in pentane (4.6 mL, 8.6 mmol, 1.9 M, 2 eq) was added dropwise over a period of 30 min. After 0.5 h at -78 °C, dry dimethylformamide (0.8 mL, 0.8 g, 10.9 mmol, 2.5 eq) was added slowly to the cooled reaction mixture. The solution was stirred for 10 min at -78 °C and then allowed to warm to approximately -40 °C for 10 min, whereon deionized water (50 mL) was added. The THF was removed under reduced pressure and DCM was added to the residue. The phases were separated and the organic layer was washed with deionized water (2 x 50 mL). The mixture was dried over magnesium sulfate and the solvent was removed under reduced pressure. The crude product was purified by silica column chromatography, using DCM as eluent. Compound **2** was isolated as lemony crystals in 74 % yield (0.83 g, 3.2 mmol).**^{1}H-NMR** (400 MHz, $CDCl_3$) δ / ppm = 9.72 (s, 1H, *H*-1), 5.08 (vt, 2H, $^3J_{HH}$ = 1.80 Hz, *H*-3), 4.86 (vt, 2H, $^3J_{HH}$ = 1.80 Hz, *H*-2), 4.65 (s, 5H, *H*-4).

Ethynylruthenocene[10]

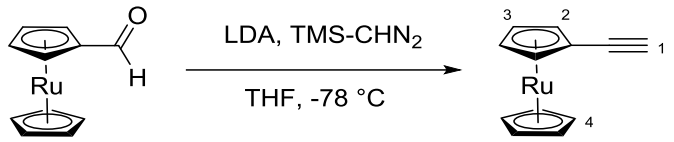

2 **3**

A prepared mixture of LDA (1.3 mL, 2 M in heptane/THF/ethylbenzene, 2.5 mmol, 1.2 eq) and dry THF (50 mL) was cooled to -78 °C. Subsequently, (trimethylsilyl)diazomethane (1.3 mL, 2 M solution in hexane, 2.5 mmol, 1.2 eq) was added slowly. The reaction was stirred for 10 min at -78 °C, whereon formylruthenocene (**2**) (0.55 g, 2.1 mmol, 1 eq), which was dissolved in dry THF (10 mL), was added dropwise. The mixture was stirred for 1 h at -78 °C, was allowed to reach RT and subsequently heated to 60 °C. The mixture was stirred at this temperature for 3 h before it was poured into a saturated solution of ammonium chloride. Organic compounds were extracted with diethyl ether and the resulting organic phase was washed with deionized water (2 x 25 mL). The organic layer was dried over magnesium sulfate and the solvents were removed under reduced pressure. The crude product was purified by silica column chromatography (hexane/benzene 2:1 *v/v*). Ethynylruthenocene was isolated as beige, sticky solid in quantitative yield (0.54 g, 2.1 mmol).**^{1}H-NMR** (400 MHz, $CDCl_3$) δ / ppm = 4.86 (vt, 2H, $^3J_{HH}$ = 1.7 Hz, *H*-3), 4.60 (s, 5H, *H*-4), 4.55 (vt, 2H, $^3J_{HH}$ = 1.7 Hz, *H*-2), 2.64 (s, 1H, *H*-1).

3. NMR Spectra

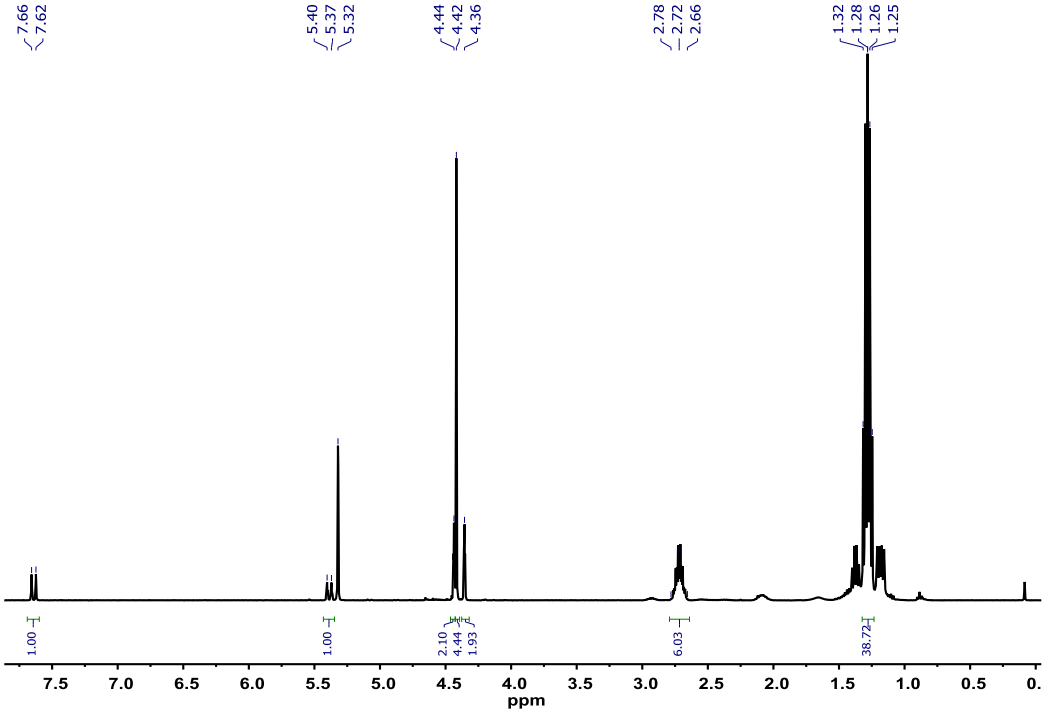

Figure S1: ^{1}H-NMR spectrum of **Rc-Ru^{Cl}** in DCM-d_2.

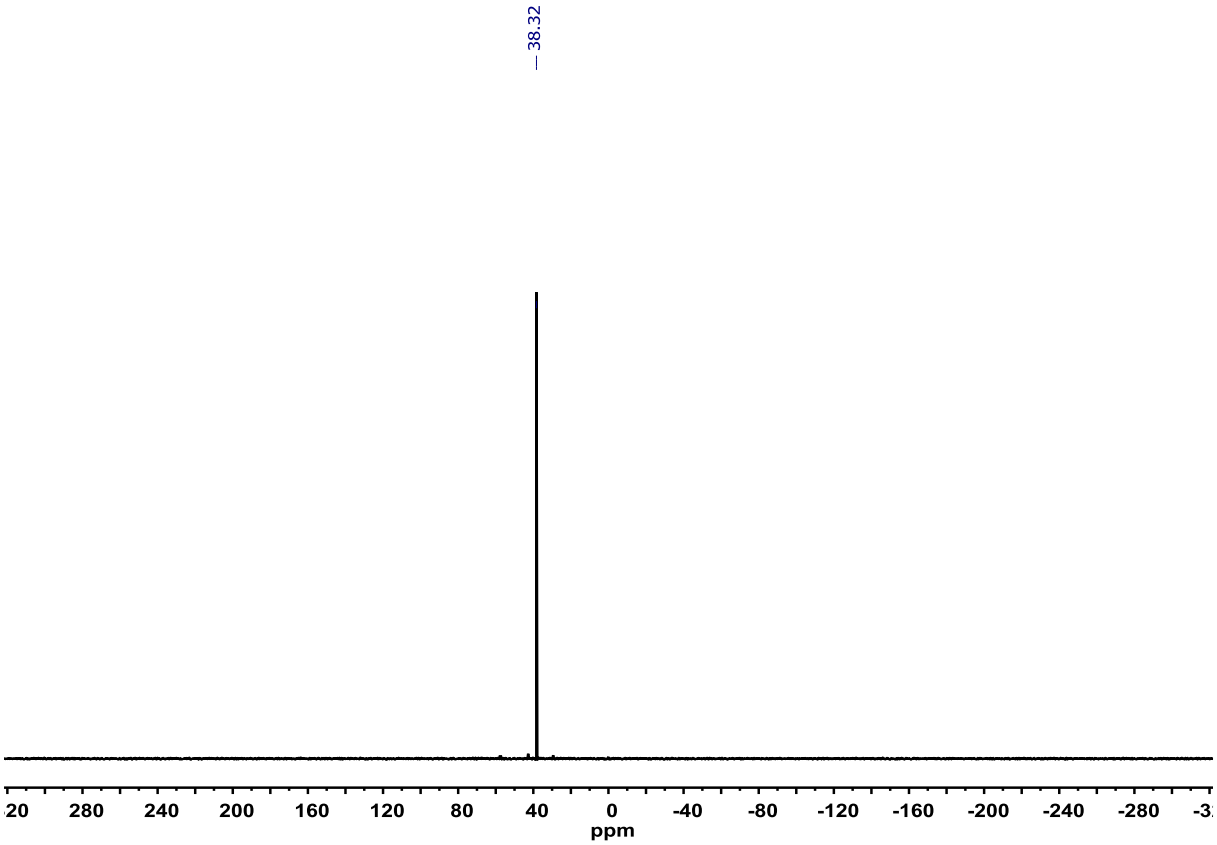

Figure S2: ^{31}P-NMR spectrum of **Rc-Ru^{Cl}** in DCM-d_2.

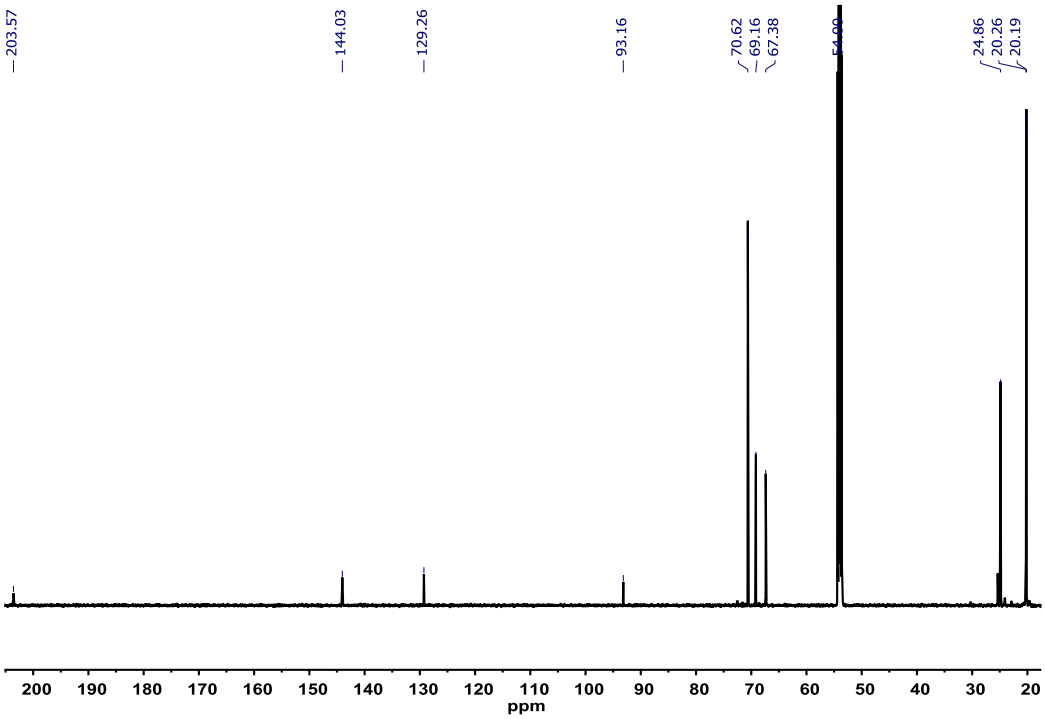

Figure S3: ^{13}C-NMR spectrum of **Rc-Ru^{Cl}** in DCM-d_2.

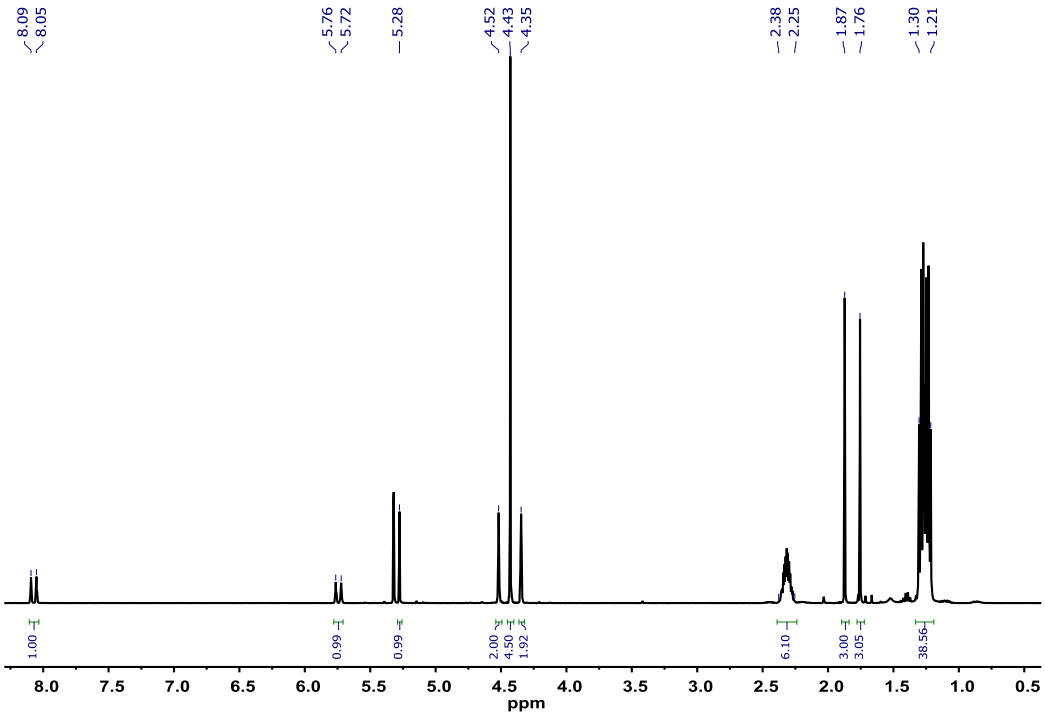

Figure S4: ^{1}H-NMR spectrum of **Rc-Ru^{acac}** in DCM-d_2.

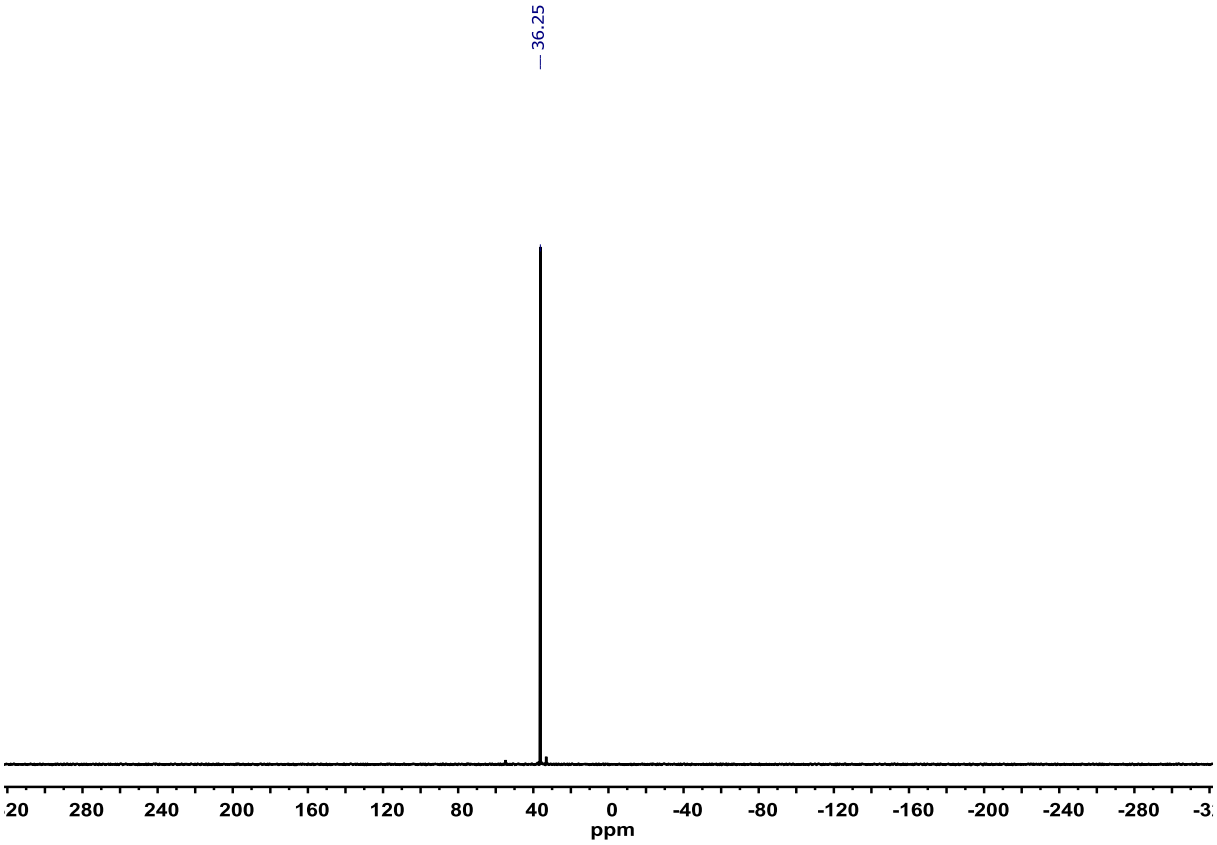

Figure S5: ^{31}P-NMR spectrum of **Rc-Ru^{acac}** in DCM-d_2.

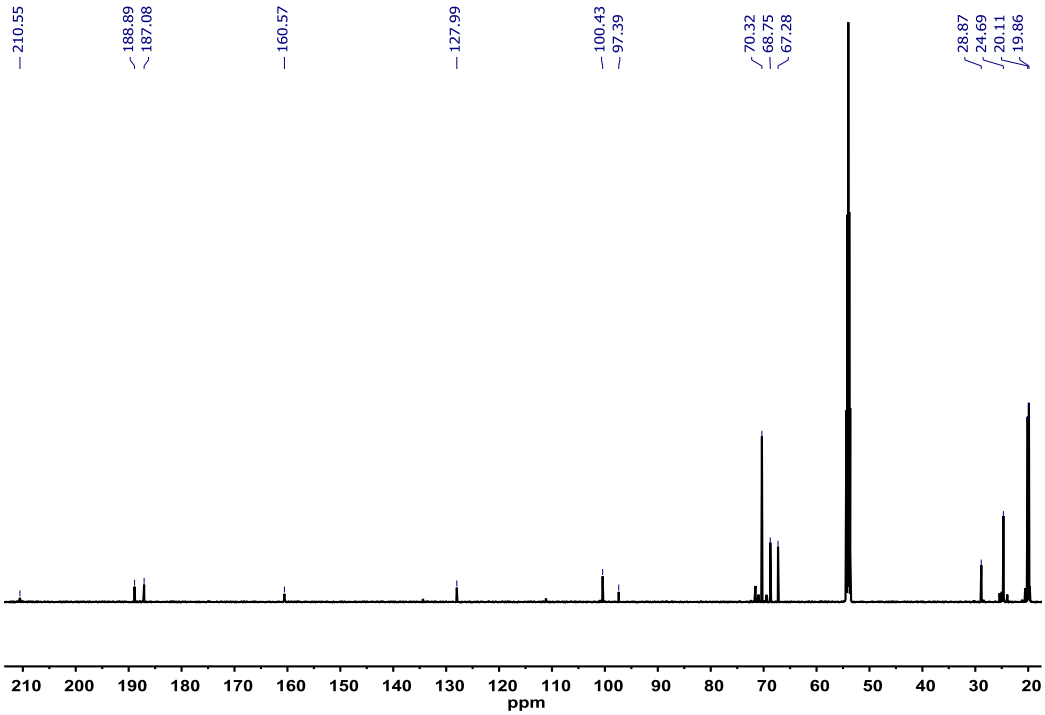

Figure S6: ^{13}C-NMR spectrum of **Rc-Ru^{acac}** in DCM-d_2.

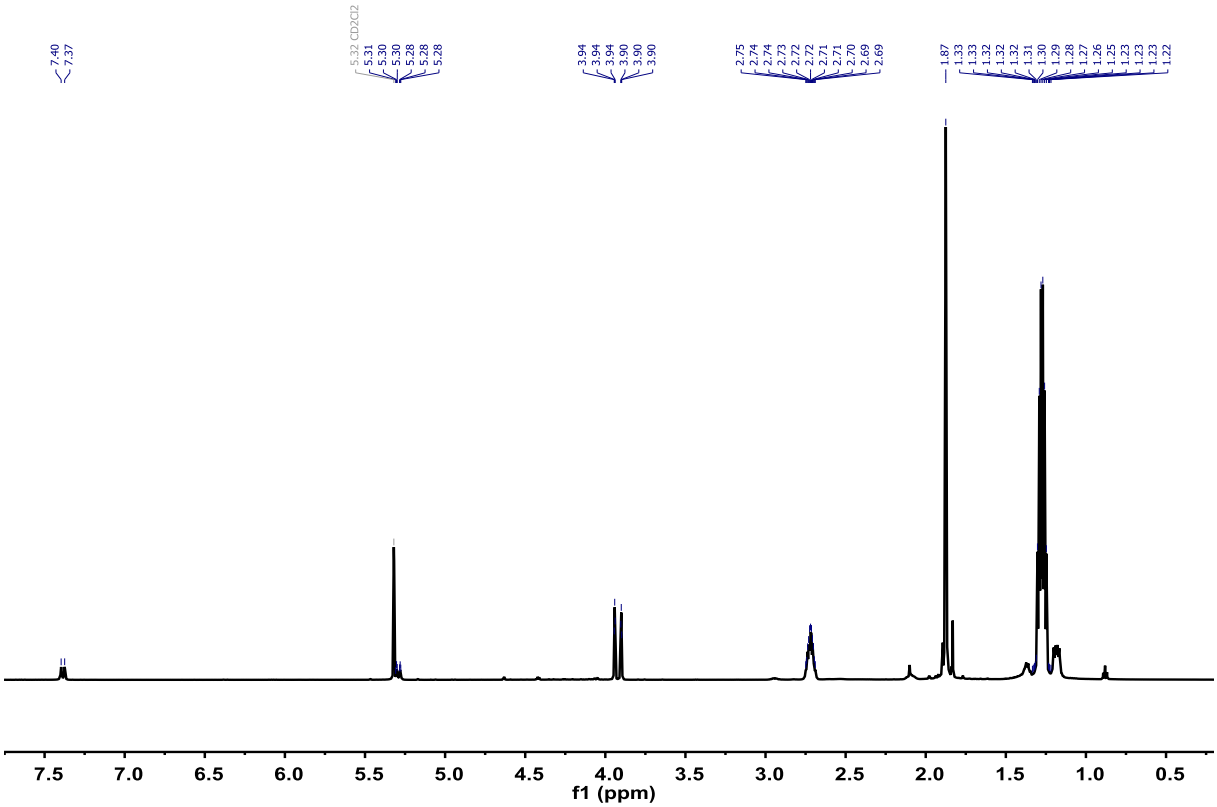

Figure S7: ^{1}H NMR of **Rc*-Ru^{Cl}** in DCM-d_2 at room temperature.

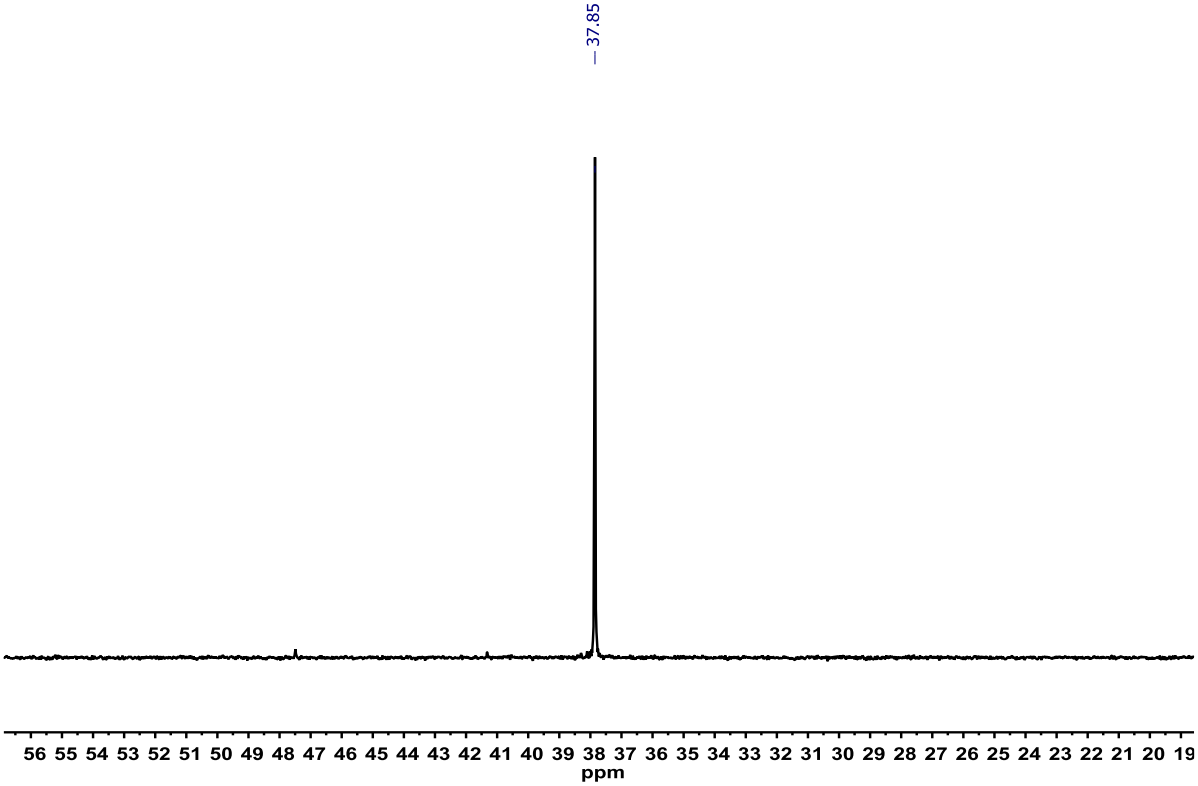

Figure S8: ^{31}P NMR of **Rc*-Ru^{Cl}** in DCM-d_2 at room temperature.

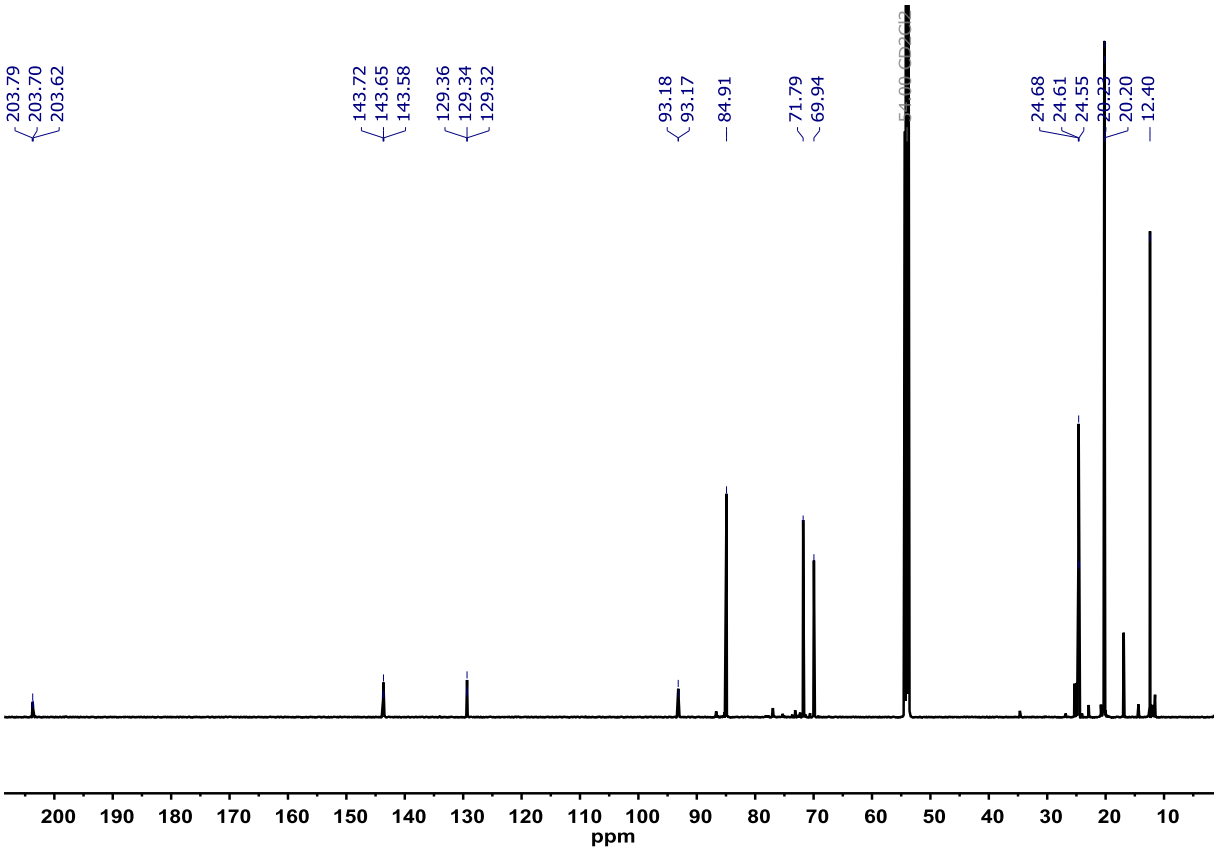

Figure S9: ^{13}C NMR of **Rc*-Ru^{Cl}** in DCM-d_2 at room temperature.

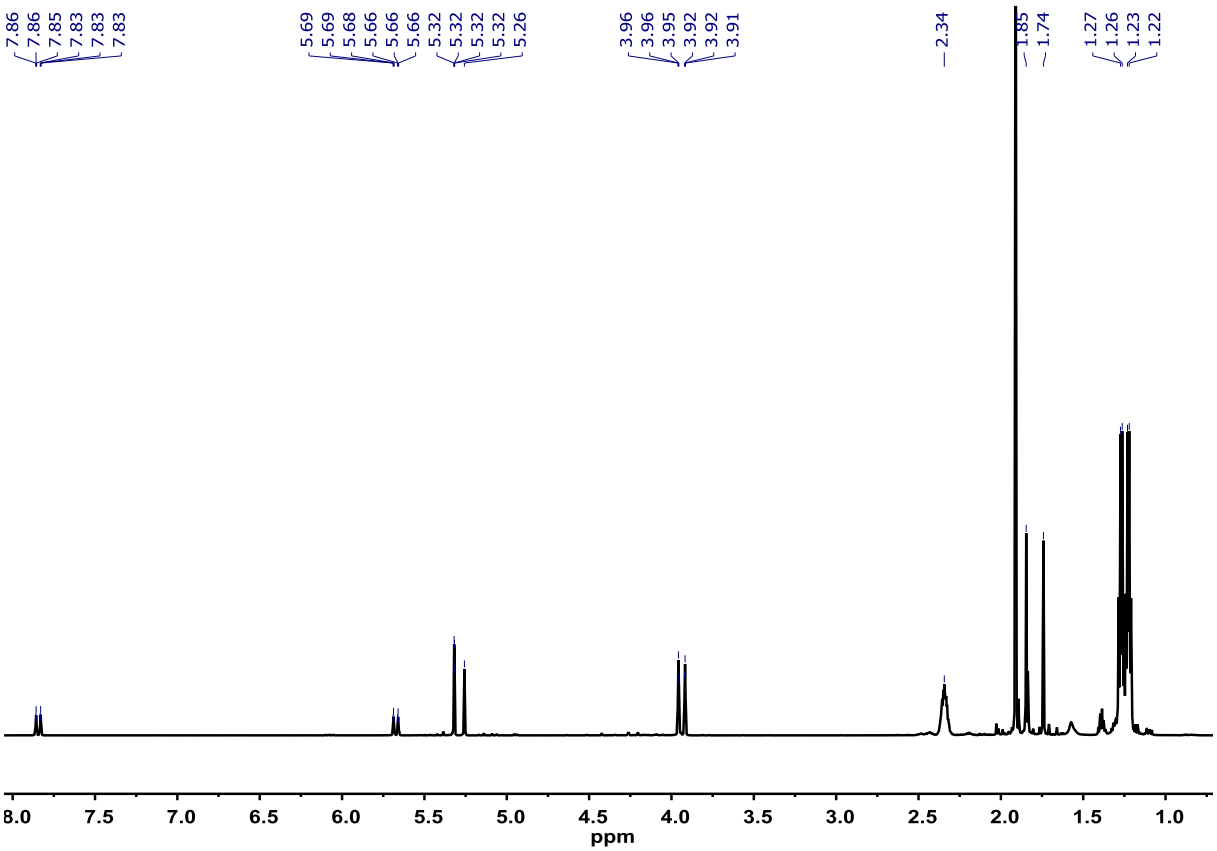

Figure S10: ^{1}H NMR of **Rc*-Ru^{acac}** in DCM-d_2 at room temperature.

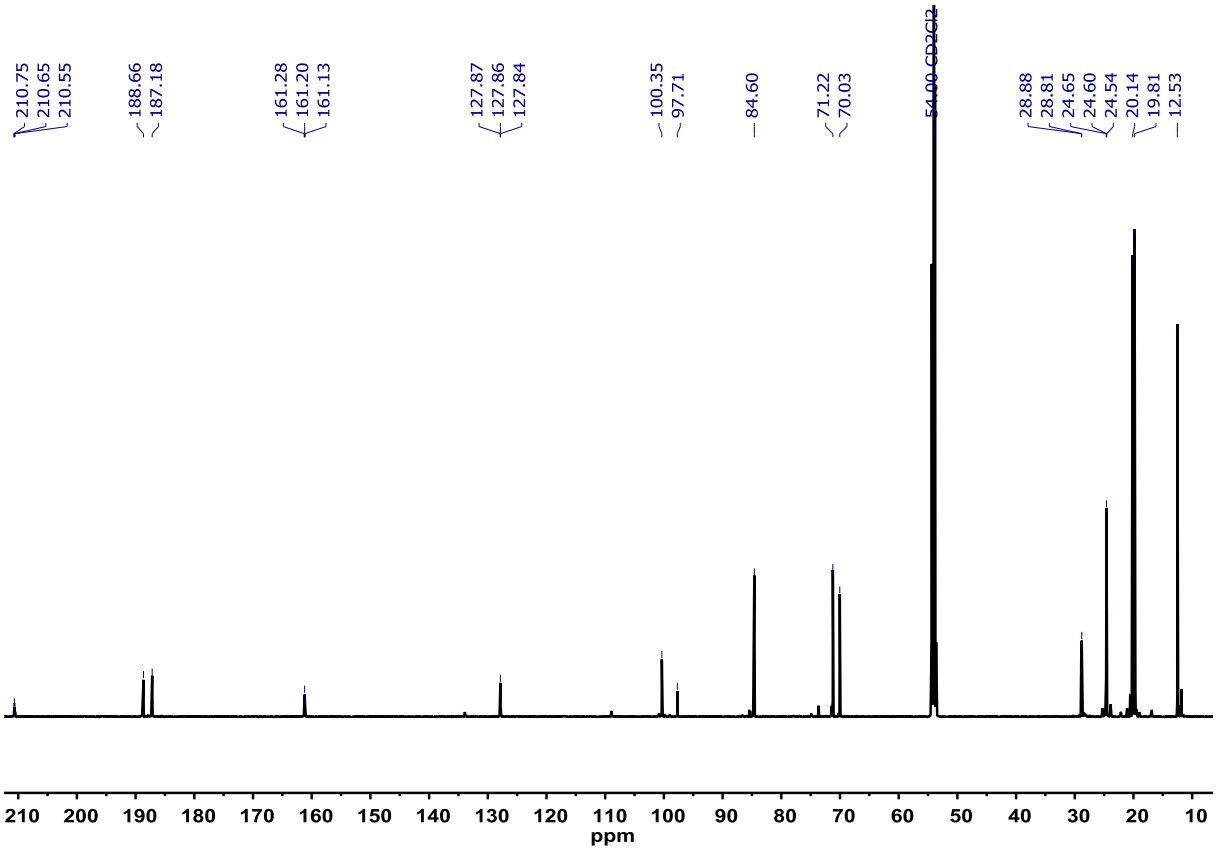

Figure S11: ^{13}C NMR of **Rc*-Ru^{acac}** in DCM-d_2 at room temperature.

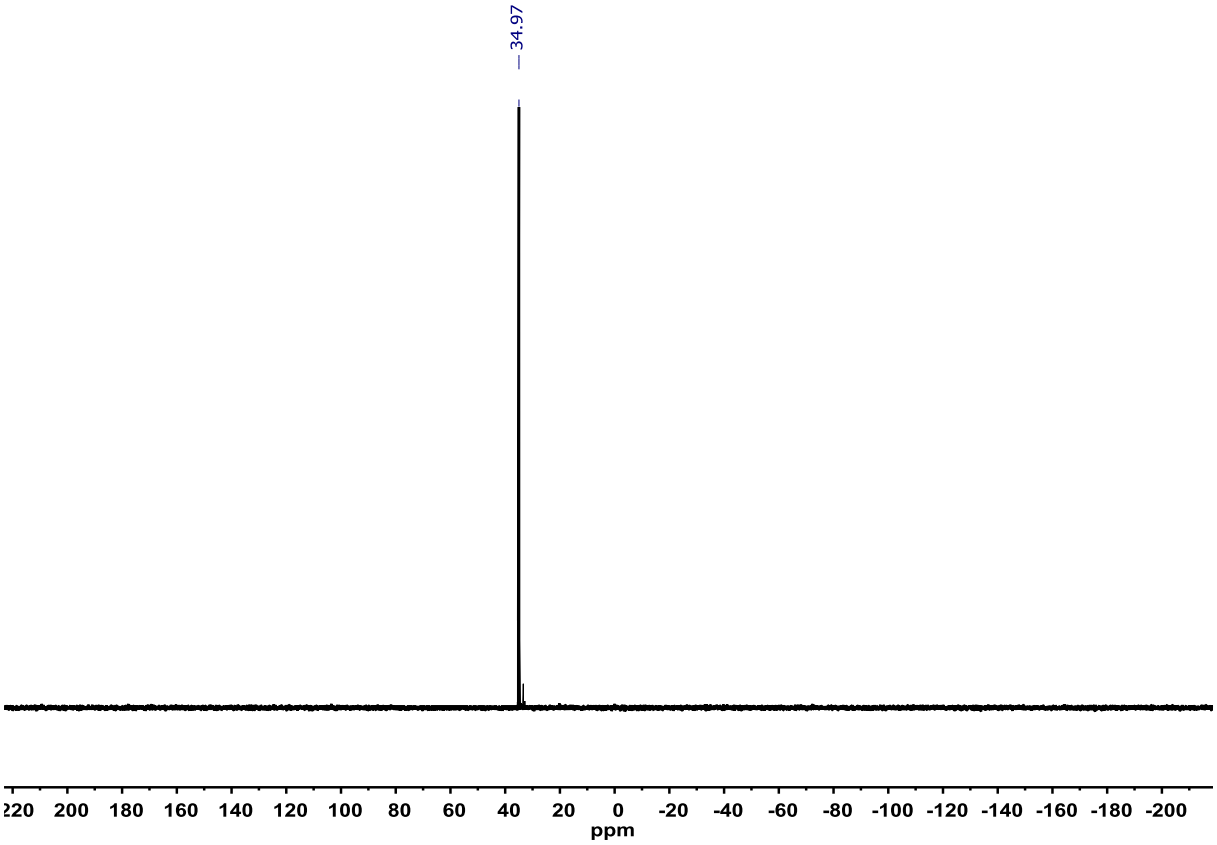

Figure S12: ^{31}P NMR of **Rc*-Ru^{acac}** in DCM-d_2 at room temperature.

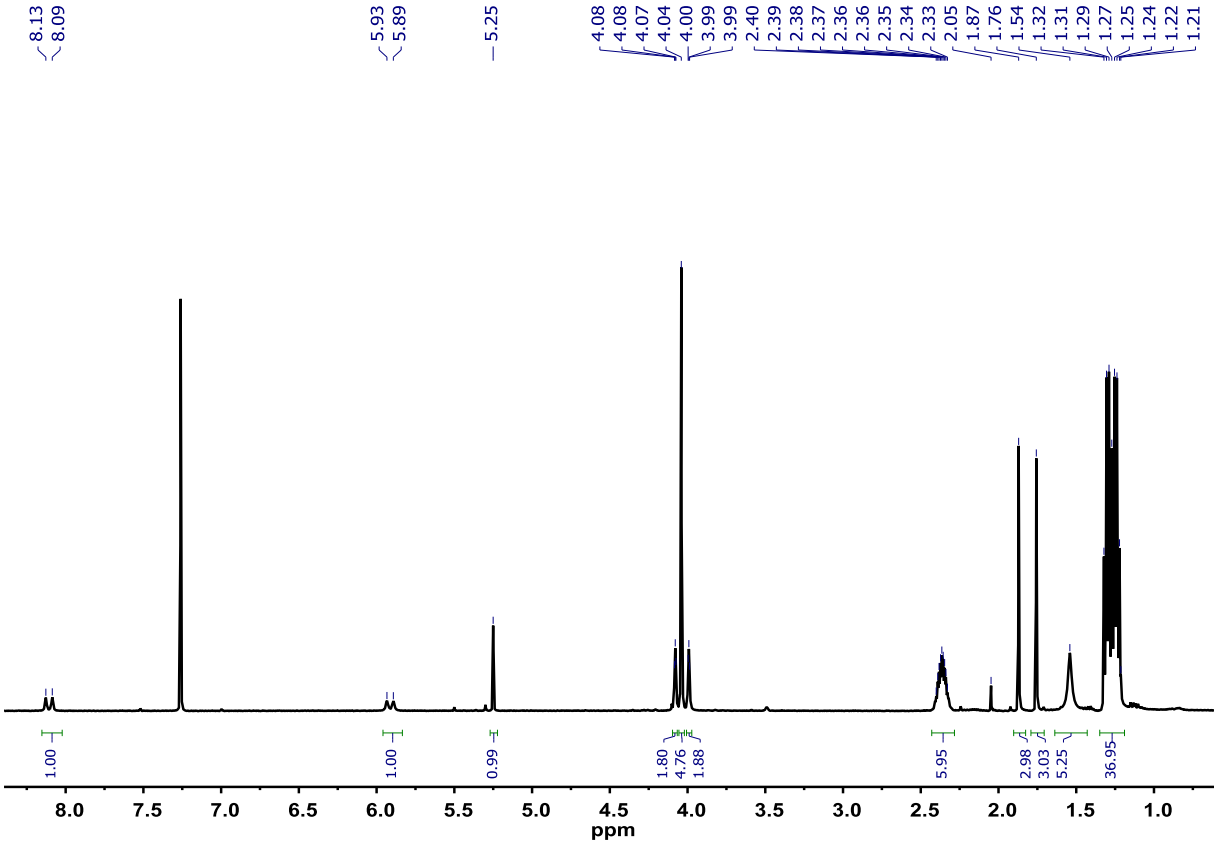

Figure S13: ^{1}H NMR of **Fc-Ru^{acac}** in $CDCl_3$ at room temperature.

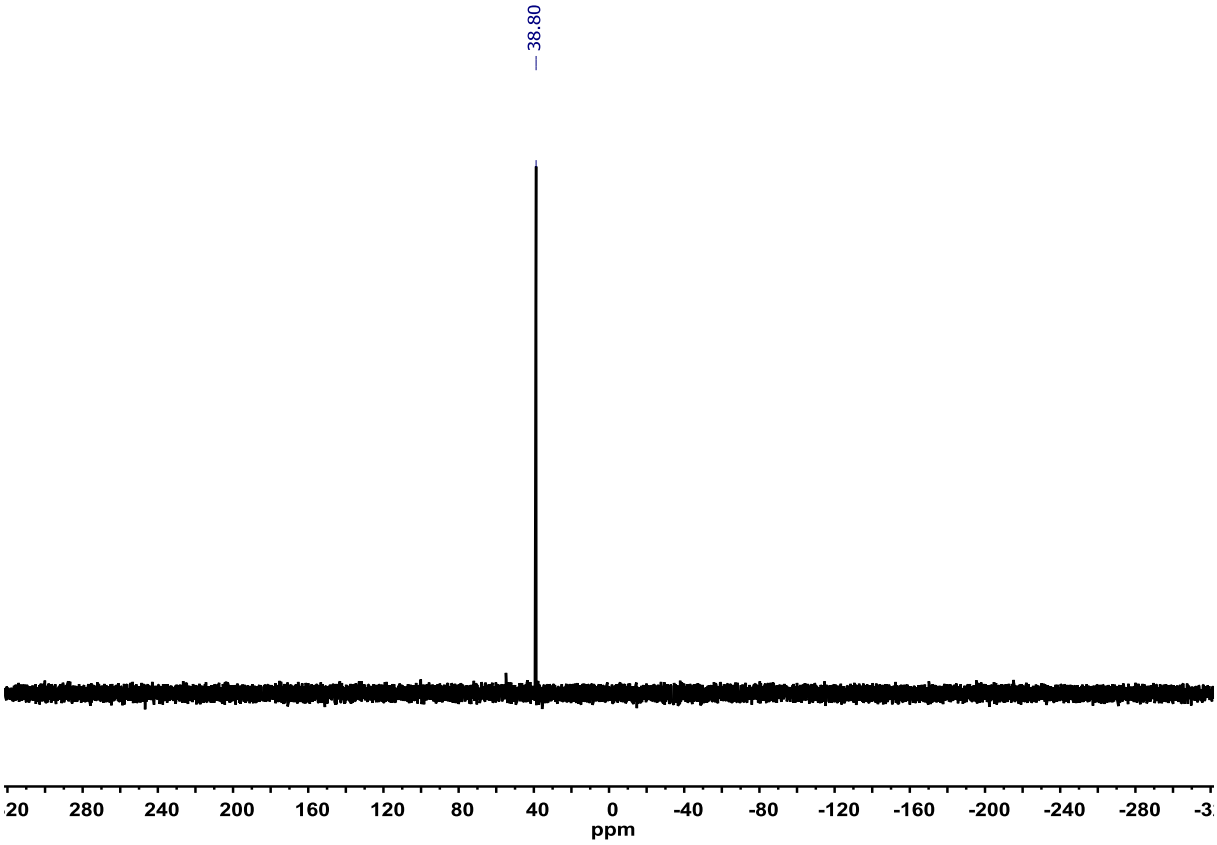

Figure S14: ^{31}P NMR of **Fc-Ru^{acac}** in $CDCl_3$ at room temperature.

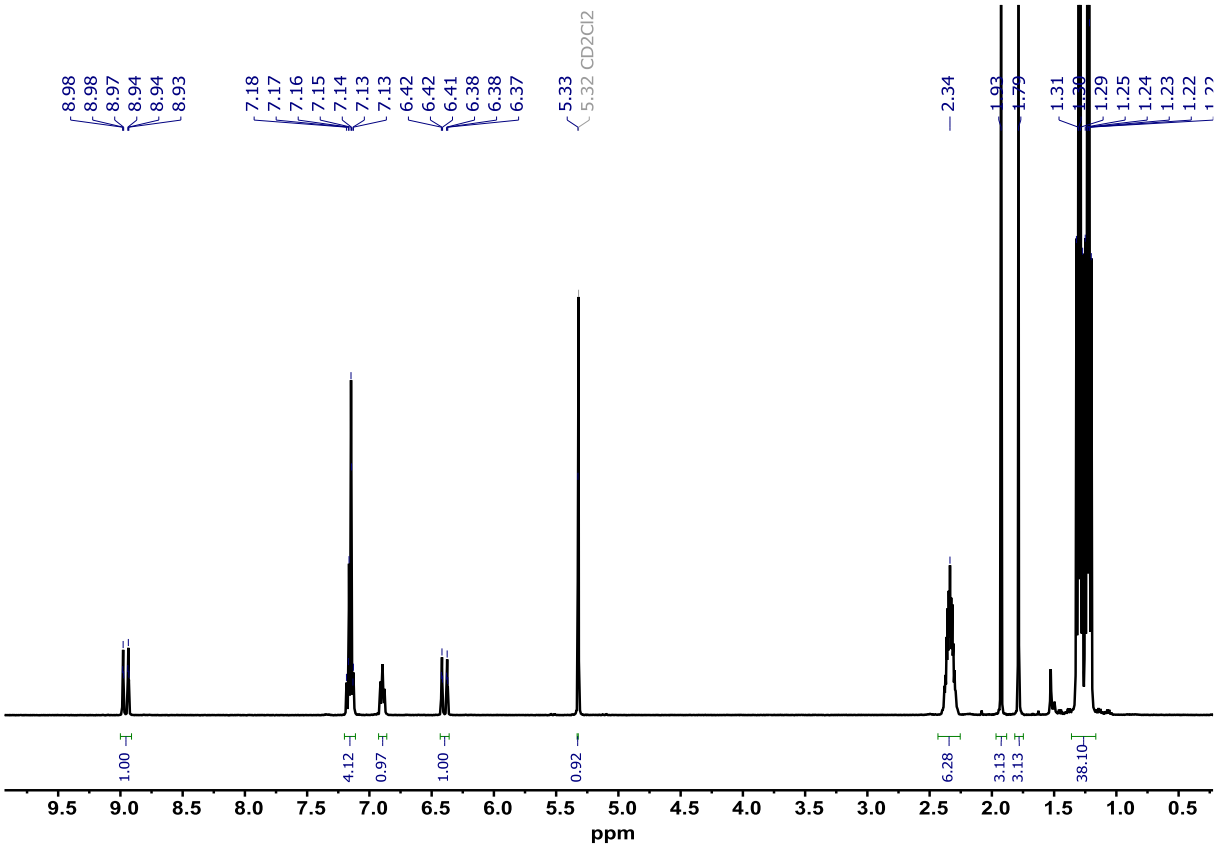

Figure S15: ^{1}H NMR of **Ph-Ru^{acac}** in $CDCl_3$ at room temperature.

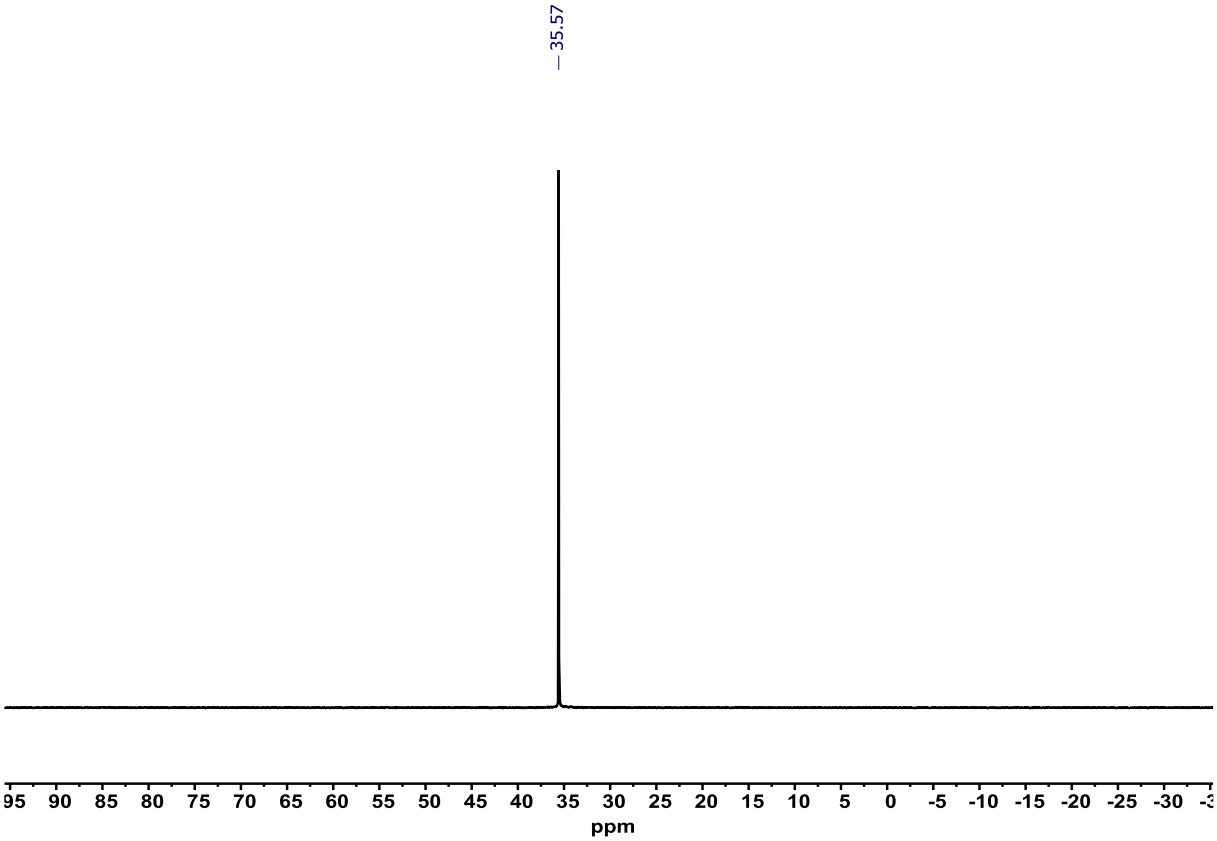

Figure S16: ^{31}P NMR of **Ph-Ru^{acac}** in $CDCl_3$ at room temperature.

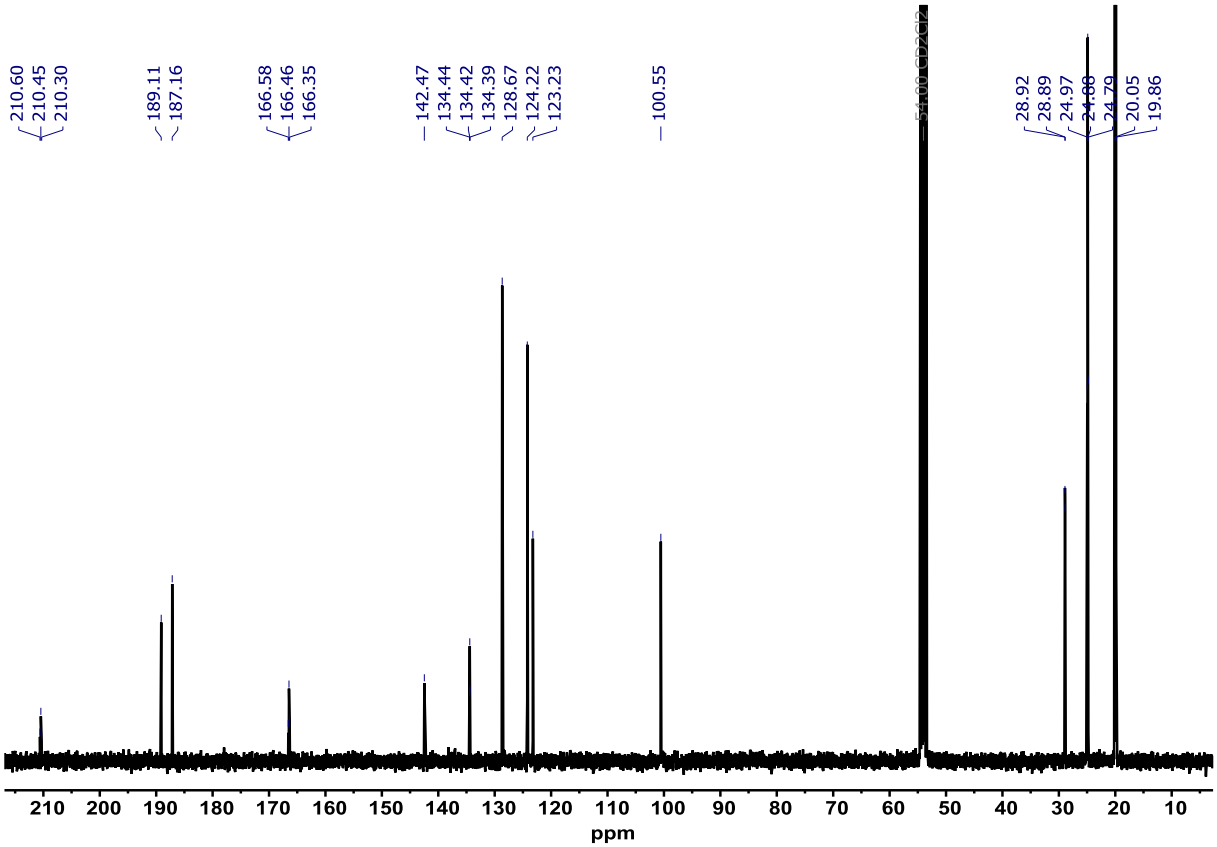

Figure S17: ^{13}C NMR of **Ph-Ru^{acac}** in $CDCl_3$ at room temperature.

4. Crystallographic data

Table S1: Crystal data and structure refinement for **Ph-Ru^{acac}**

Empirical formula	$C_{32}H_{56}O_3P_2Ru$
Formula weight	651.77
Temperature/K	100.15
Crystal system	triclinic
Space group	P-1
a/Å	10.5425(9)
b/Å	11.0929(9)
c/Å	14.8950(13)
α/°	91.934(7)
β/°	93.831(7)
γ/°	99.302(7)
Volume/Å^3	1713.4(3)
Z	2
ρ_{calc}g/cm^3	1.263
μ/mm^{-1}	0.579
F(000)	692.0
Crystal size/mm^3	0.01 × 0.2 × 0.3, light yellow plate
Radiation	MoKα (λ = 0.71073)
2Θ range for data collection/°	3.724 to 58.398
Index ranges	-14 ≤ h ≤ 14, -13 ≤ k ≤ 15, -20 ≤ l ≤ 20
Reflections collected	31843
Independent reflections	9227 [R_{int} = 0.0367, R_{sigma} = 0.0292]
Data/restraints/parameters	9227/0/358
Goodness-of-fit on F^2	1.036
Final R indexes [I>=2σ (I)]	R_1 = 0.0491, wR_2 = 0.1259
Final R indexes [all data]	R_1 = 0.0579, wR_2 = 0.1319
Largest diff. peak/hole / e Å^{-3}	1.29/-0.86

Table S2: Fractional Atomic Coordinates (×10^4) and Equivalent Isotropic Displacement Parameters (Å^2×10^3) for Ph-Ru^{acac}. U_{eq} is defined as 1/3 of of the trace of the orthogonalised U_{IJ} tensor**.**

Atom	***x***	***y***	***z***	**U(eq)**
Ru1	7045.7(2)	7161.2(2)	7514.3(2)	23.78(8)
P1	8087.1(7)	5368.0(6)	7313.7(5)	29.63(14)
P2	6028.6(6)	8960.7(6)	7615.1(4)	25.28(13)
O1	6765.5(17)	6869.1(17)	8935.0(12)	29.8(4)
O2	8873.0(16)	8166.3(16)	7990.1(12)	26.9(3)
O3	4496.7(18)	5737.9(18)	6858.4(15)	38.1(4)
C1	7539(2)	7643(2)	6265.9(16)	25.7(4)
C2	6956(2)	7374(2)	5440.4(17)	29.1(5)
C3	7452(2)	7798(2)	4584.9(17)	28.4(5)
C4	7023(2)	7104(2)	3790.4(17)	30.9(5)
C5	7449(3)	7468(3)	2961.7(18)	34.8(5)
C6	8310(3)	8539(3)	2903.7(18)	36.3(6)
C7	8751(3)	9251(3)	3687.0(19)	35.8(5)
C8	8326(3)	8884(3)	4517.6(18)	32.5(5)
C9	7935(3)	4714(3)	6129.4(19)	35.8(5)
C10	6555(3)	4218(3)	5763(2)	44.7(7)
C11	8799(4)	3759(3)	5925(2)	48.5(7)
C12	7549(3)	4064(3)	8034(2)	38.6(6)
C13	6080(4)	3742(3)	8011(3)	51.5(8)
C14	8095(5)	4308(3)	9019(2)	58.7(10)
C15	9867(3)	5731(3)	7597(2)	38.5(6)
C16	10609(4)	4655(4)	7755(3)	60.0(10)
C17	10520(3)	6573(3)	6920(2)	43.9(7)
C18	5105(3)	9244(2)	6544.7(18)	32.4(5)
C19	3754(3)	8480(3)	6410(2)	41.3(6)
C20	5013(3)	10580(3)	6350(2)	38.2(6)
C21	7129(2)	10451(2)	7844.2(17)	28.7(5)
C22	8185(2)	10601(2)	7182.8(19)	32.5(5)
C23	7712(3)	10648(2)	8820.2(19)	33.7(5)
C24	4976(2)	8943(2)	8577.4(17)	29.5(5)
C25	4293(3)	10061(3)	8658(2)	35.4(5)
C26	4031(3)	7750(3)	8635(2)	35.9(5)
C27	7569(3)	7199(2)	9601.0(18)	32.7(5)
C28	8848(3)	7794(3)	9564.3(18)	34.4(5)
C29	9409(2)	8236(2)	8788.5(18)	30.9(5)
C30	7089(3)	6916(3)	10515.9(19)	41.9(6)
C31	10778(3)	8915(3)	8886(2)	38.4(6)
C32	5500(3)	6294(2)	7096.6(18)	30.8(5)

Table S3: Anisotropic Displacement Parameters ($Å^2 \times 10^3$) for Ph-Ru^{acac}. The Anisotropic displacement factor exponent takes the form: $-2\pi^2[h^2a^{*2}U_{11}+2hka^*b^*U_{12}+\ldots]$.

Atom	**U_{11}**	**U_{22}**	**U_{33}**	**U_{23}**	**U_{13}**	**U_{12}**
Ru1	23.49(11)	24.39(12)	23.77(11)	1.26(7)	2.60(7)	4.51(7)
P1	33.2(3)	27.7(3)	29.6(3)	1.4(2)	4.8(2)	8.5(2)
P2	22.8(3)	26.4(3)	27.1(3)	1.3(2)	2.8(2)	4.9(2)
O1	31.8(8)	33.3(9)	25.9(8)	4.1(7)	4.7(6)	8.2(7)
O2	22.2(7)	29.1(8)	28.9(8)	0.5(7)	-0.6(6)	3.9(6)
O3	29.7(9)	33.6(10)	48.3(12)	-6.5(8)	-0.7(8)	0.0(7)
C1	26.7(10)	27.4(11)	24.2(10)	2.7(8)	4.8(8)	6.0(8)
C2	27.7(11)	28.2(11)	31.0(12)	2.2(9)	2.4(9)	2.9(9)
C3	26.1(10)	31.5(12)	28.6(11)	2.3(9)	2.7(8)	7.4(9)
C4	31.9(12)	31.8(12)	29.2(12)	1.9(9)	3.2(9)	5.9(9)
C5	35.9(13)	42.2(14)	27.8(12)	-0.1(10)	2.5(9)	11.4(11)
C6	34.8(13)	48.4(15)	29.1(12)	9.2(11)	9.0(10)	12.5(11)
C7	31.3(12)	40.2(14)	35.7(13)	7.0(11)	5.7(10)	2.8(10)
C8	31.2(12)	36.0(13)	30.1(12)	3.1(10)	2.0(9)	5.0(10)
C9	45.3(14)	31.3(12)	32.1(13)	-1.4(10)	7.7(10)	9.1(11)
C10	46.7(16)	44.2(16)	41.7(15)	-9.2(13)	4.3(12)	5.1(13)
C11	62(2)	43.5(16)	44.4(16)	-4.7(13)	11.2(14)	21.3(15)
C12	52.0(16)	28.5(12)	38.9(14)	8.6(10)	10.8(12)	13.0(11)
C13	57.2(19)	41.6(16)	61(2)	17.0(15)	25.6(16)	10.7(14)
C14	103(3)	38.5(16)	37.7(16)	11.0(13)	6.6(17)	18.0(18)
C15	32.5(12)	40.9(15)	44.4(15)	-1.7(12)	-1.7(11)	16.1(11)
C16	51.8(19)	59(2)	76(3)	2.1(19)	-6.0(17)	32.4(17)
C17	30.5(13)	50.4(17)	50.9(17)	-3.5(14)	5.5(12)	7.0(12)
C18	32.9(12)	36.4(13)	29.3(12)	2.6(10)	-1.4(9)	11.2(10)
C19	35.4(13)	41.9(15)	45.0(16)	-1.1(12)	-12.4(11)	8.8(12)
C20	37.6(13)	38.4(14)	41.1(14)	9.4(11)	0.4(11)	13.4(11)
C21	27.9(11)	25.3(11)	34.0(12)	1.2(9)	4.2(9)	6.6(9)
C22	28.1(11)	29.6(12)	40.1(14)	3.6(10)	6.6(10)	3.7(9)
C23	32.1(12)	30.2(12)	37.8(13)	-5.1(10)	-0.5(10)	4.8(10)
C24	27.0(11)	32.3(12)	30.7(11)	0.8(9)	8.1(9)	7.1(9)
C25	32.4(12)	34.7(13)	41.2(14)	-0.2(11)	10.2(10)	9.4(10)
C26	29.8(12)	35.6(13)	42.8(14)	4.3(11)	9.0(10)	4.3(10)
C27	38.8(13)	32.7(12)	28.9(12)	3.5(10)	4.5(10)	11.3(10)
C28	38.1(13)	39.1(14)	26.8(11)	-0.6(10)	-3.5(10)	12.1(11)
C29	29.6(11)	30.3(12)	33.5(12)	-0.3(10)	-1.0(9)	9.4(9)
C30	47.7(16)	52.7(17)	28.8(13)	6.7(12)	6.7(11)	16.0(14)
C31	30.6(12)	44.8(15)	38.1(14)	-0.3(12)	-3.6(10)	4.1(11)
C32	33.9(12)	28.5(11)	31.5(12)	2.8(9)	5.4(9)	7.8(10)

Table S4: Bond Lengths and Bond Angles for **Ph-Ru^{acac} .**

Atom	Atom	Length/Å	Atom	Atom	Length/Å	Atom	Atom	Length/Å
Ru1	P1	2.4416(7)	O2	C29	1.276(3)	C12	C14	1.539(5)
Ru1	P2	2.4188(6)	O3	C32	1.162(3)	C15	C16	1.545(4)
Ru1	O1	2.1838(18)	C1	C2	1.339(3)	C15	C17	1.521(5)
Ru1	O2	2.1276(17)	C2	C3	1.473(4)	C18	C19	1.532(4)
Ru1	C1	2.030(2)	C3	C4	1.397(3)	C18	C20	1.537(4)
Ru1	C32	1.813(3)	C3	C8	1.404(4)	C21	C22	1.528(4)
P1	C9	1.871(3)	C4	C5	1.392(4)	C21	C23	1.535(4)
P1	C12	1.867(3)	C5	C6	1.383(4)	C24	C25	1.536(4)
P1	C15	1.871(3)	C6	C7	1.396(4)	C24	C26	1.531(4)
P2	C18	1.875(3)	C7	C8	1.395(4)	C27	C28	1.408(4)
P2	C21	1.866(3)	C9	C10	1.526(4)	C27	C30	1.510(4)
P2	C24	1.869(2)	C9	C11	1.541(4)	C28	C29	1.400(4)
O1	C27	1.264(3)	C12	C13	1.530(5)	C29	C31	1.512(4)

Atom	Atom	Atom	Angle/˚	Atom	Atom	Atom	Angle/˚
P2	Ru1	P1	176.44(2)	C8	C3	C2	123.5(2)
O1	Ru1	P1	94.00(5)	C5	C4	C3	121.4(3)
O1	Ru1	P2	89.56(5)	C6	C5	C4	120.5(3)
O2	Ru1	P1	88.32(5)	C5	C6	C7	119.2(3)
O2	Ru1	P2	92.05(5)	C8	C7	C6	120.2(3)
O2	Ru1	O1	85.14(7)	C7	C8	C3	121.1(2)
C1	Ru1	P1	88.10(7)	C10	C9	P1	114.6(2)
C1	Ru1	P2	88.39(7)	C10	C9	C11	109.0(2)
C1	Ru1	O1	170.96(8)	C11	C9	P1	116.2(2)
C1	Ru1	O2	86.13(8)	C13	C12	P1	112.3(2)
C32	Ru1	P1	91.06(8)	C13	C12	C14	109.0(3)
C32	Ru1	P2	88.53(8)	C14	C12	P1	112.3(2)
C32	Ru1	O1	95.44(10)	C16	C15	P1	118.1(2)
C32	Ru1	O2	179.18(9)	C17	C15	P1	111.1(2)
C32	Ru1	C1	93.31(11)	C17	C15	C16	110.1(3)
C9	P1	Ru1	114.17(9)	C19	C18	P2	114.1(2)
C12	P1	Ru1	115.69(9)	C19	C18	C20	108.8(2)
C12	P1	C9	106.14(13)	C20	C18	P2	117.13(19)
C12	P1	C15	103.76(14)	C22	C21	P2	110.64(17)
C15	P1	Ru1	111.92(9)	C22	C21	C23	110.9(2)
C15	P1	C9	103.99(13)	C23	C21	P2	113.78(18)
C18	P2	Ru1	113.42(8)	C25	C24	P2	114.38(19)
C21	P2	Ru1	116.31(8)	C26	C24	P2	114.32(18)
C21	P2	C18	101.91(12)	C26	C24	C25	111.3(2)
C21	P2	C24	101.50(11)	O1	C27	C28	126.2(3)
C24	P2	Ru1	112.62(8)	O1	C27	C30	115.8(3)
C24	P2	C18	110.00(12)	C28	C27	C30	118.0(2)
C27	O1	Ru1	127.40(18)	C29	C28	C27	125.6(2)
C29	O2	Ru1	127.82(17)	O2	C29	C28	126.9(2)
C2	C1	Ru1	133.1(2)	O2	C29	C31	114.8(2)
C1	C2	C3	126.5(2)	C28	C29	C31	118.2(2)
C4	C3	C2	119.0(2)	O3	C32	Ru1	177.7(2)
C4	C3	C8	117.6(2)				

5. Cyclic Voltammetry

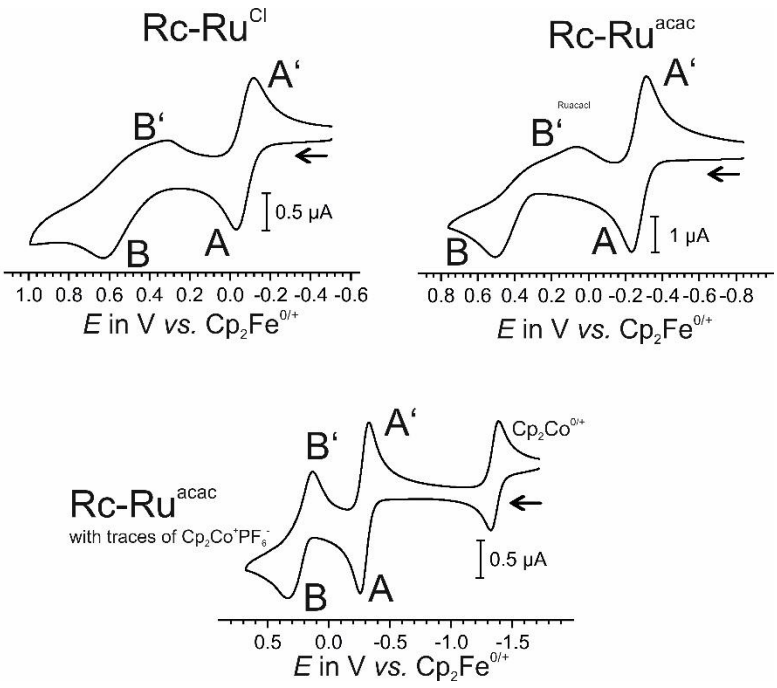

Figure S18: Cyclic voltammograms of **Rc-Ru^{Cl}** and **Rc-Ru^{acac}** in CH_2Cl_2 and NBu_4^+ $[B\{C_6H_3(CF_3)_2\text{-}3,5\}_4]^-$ as supporting electrolyte at room temperature.

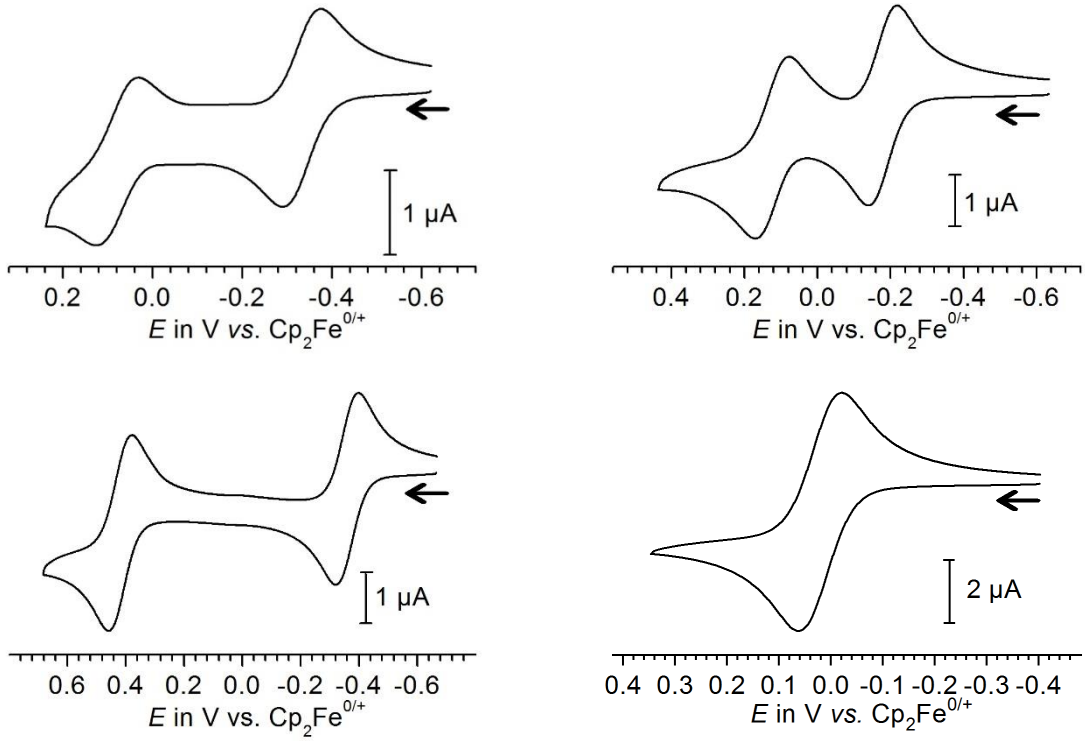

Figure S19: Cyclic voltammograms of **Rc*-Ru^{Cl}** (top left) and **Rc-Ru^{acac}** (top right) and **Fc-Ru^{acac}**(bottom left) and **Ph-Ru^{acac}** (bottom right), vs FcH/FcH+ in CH_2Cl_2/NBu_4PF_6 (0.1 M) at r.t. and v = 100 mV/s

6. IR Spectroelectrochemistry

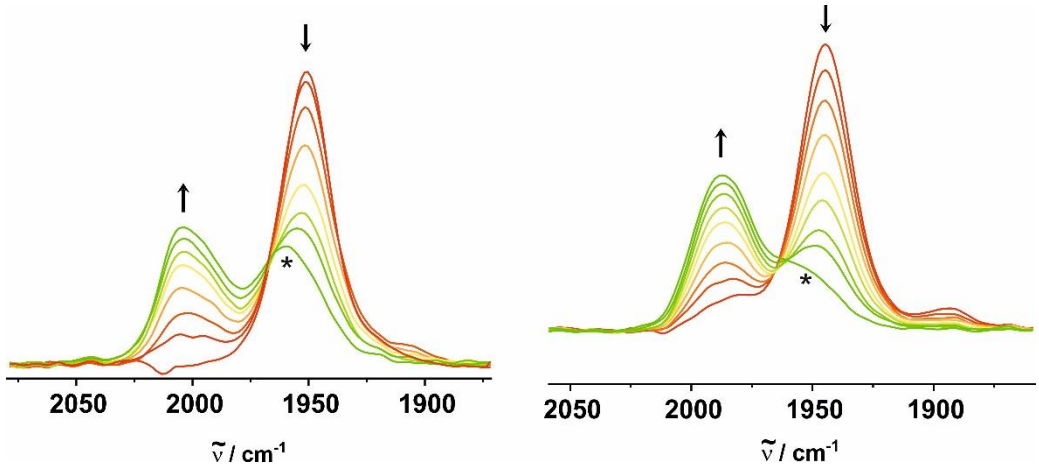

Figure S20: IR-spectroelectrochemical changes during oxidation of **Rc-Ru^{Cl}** and **Rc-Ru^{acac}** in dichloromethane and NBu_4PF_6 as supporting electrolyte (0.1 M) at room temperature red cationic and green dicationic form. The asterisk marks the decomposition product.

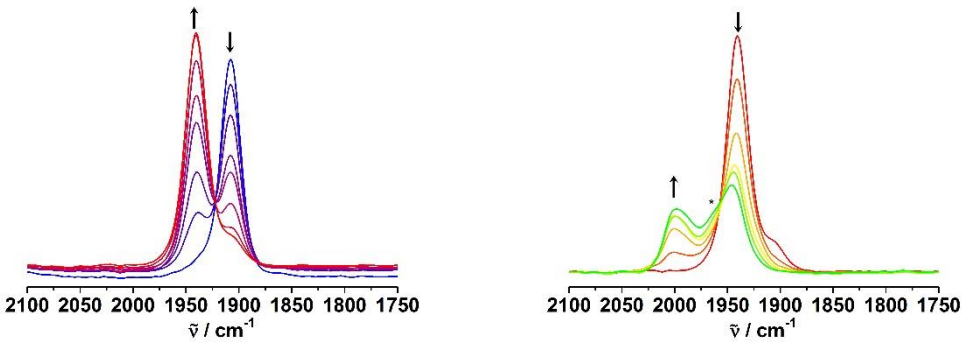

Figure S21: IR-spectroelectrochemical changes during oxidation of **Rc*-Ru^{Cl}** in dichloromethane and NBu_4PF_6 as supporting electrolyte (0.1 M) at room temperature, blue neutral, red cationic and green dicationic form. The asterisk marks the decomposition product.

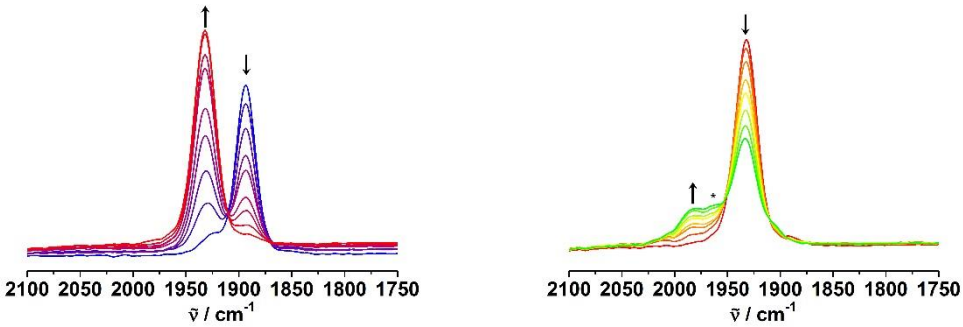

Figure S22. IR-spectroelectrochemical changes during oxidation of **Rc*-Ru^{acac}** in dichloromethane and NBu_4PF_6 as supporting electrolyte (0.1 M) at room temperature, blue neutral, red cationic and green dicationic form. The asterisk marks the decomposition product.

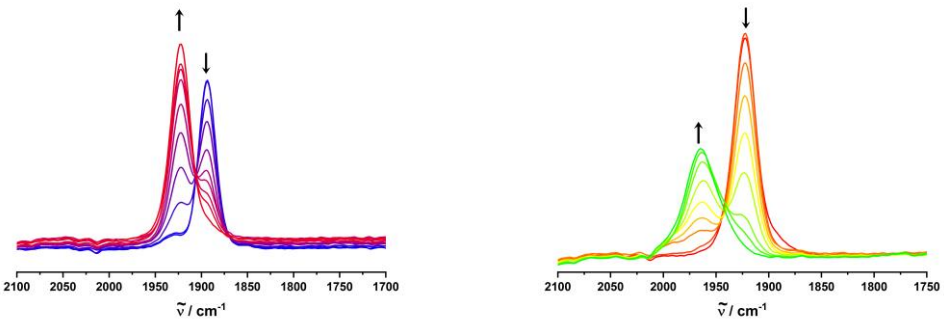

Figure S23: IR-spectroelectrochemical changes during oxidation of **Fc-Ru^{acac}** in dichloromethane and NBu_4PF_6 as supporting electrolyte (0.1 M) at room temperature, blue neutral, red cationic and green dicationic form.

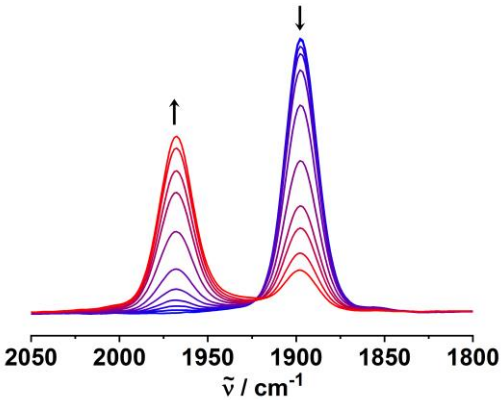

Figure S24: IR-spectroelectrochemical changes during oxidation of **Ph-Ru^{acac}** in dichloromethane and NBu_4PF_6 as supporting electrolyte (0.1 M) at room temperature, blue neutral, red cationic form.

7. (TD-)DFT calculations

Molecular Orbitals and calculated transitions

neutral state	oxidized state	
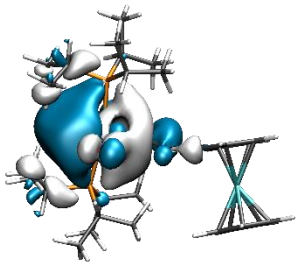 LUMO, E = -1.45 eV	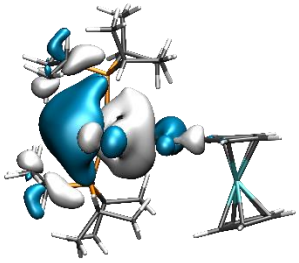 α-LUSO, E = -2.42 eV	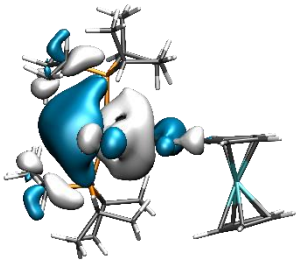 β-LUSO+1, E = -2.36 eV
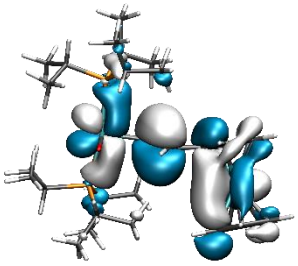 HOMO, E = -5.13 eV	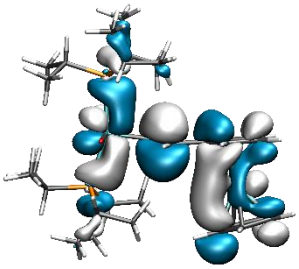 α-HOSO, E = -6.19 eV	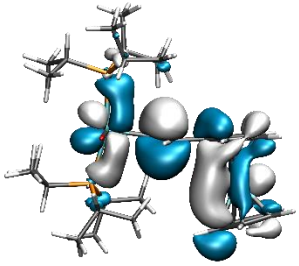 β-LUSO, E = -4.17 eV
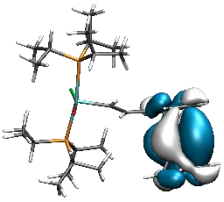 HOMO-1, E = -5.80 eV		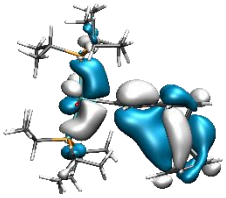 β-HOSO, E = -6.62 eV
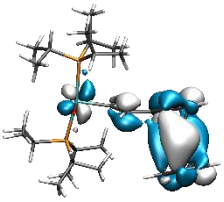 HOMO-2, E = -5.86 eV		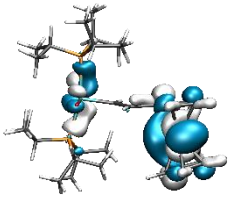 β-HOSO-1, E = -6.93 eV
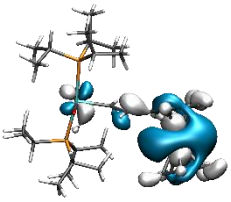 HOMO-3, E = -6.02 eV		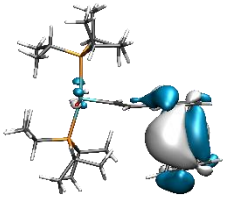 β-HOSO-2, E = -6.97 eV

Figure S25: Molecular orbitals for **Rc-Ru^{Cl}** in its neutral and oxidized states.

neutral state	oxidized state	
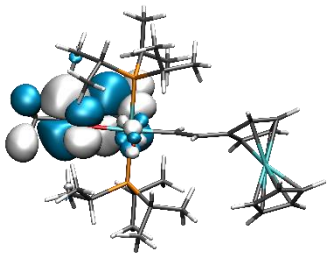	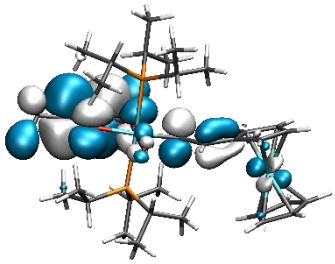	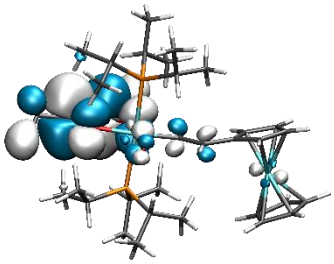
LUMO, E = -0.77 eV	α-LUSO, E = -1.38 eV	β-LUSO+1, E = -1.35eV
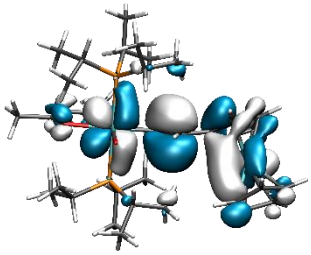	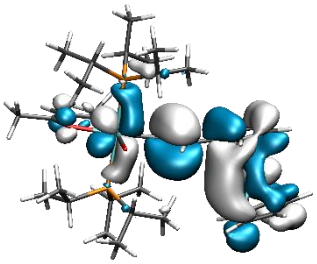	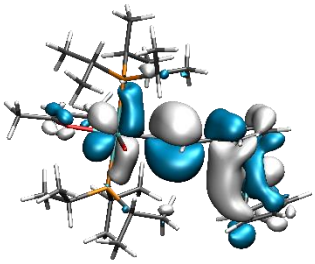
HOMO, E = -4.96eV	α-HOSO, E = -6.14 eV	β-LUSO, E = -4.06 eV
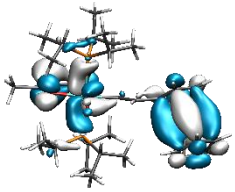	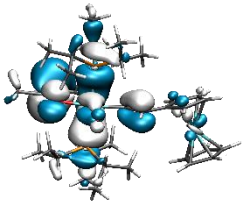	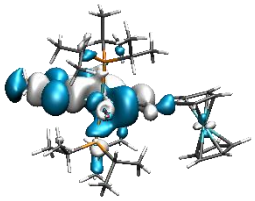
HOMO-1, E = -5.71 eV	β-HOSO-1, E = - eV	β-HOSO-5, E = - eV
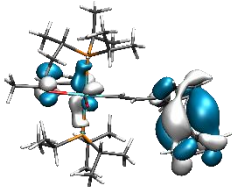	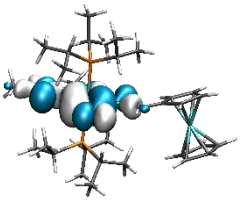	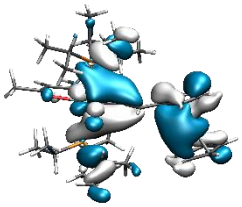
HOMO-2, E = -5.73 eV	β-HOSO-2, E = - eV	β-HOSO-6, E = - eV
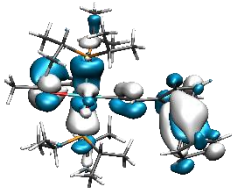	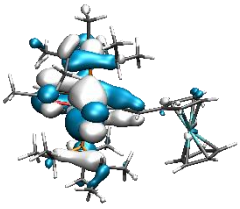	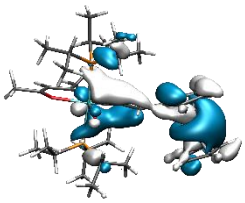
HOMO-3, E = -5.82 eV	β-HOSO-4, E = - eV	β-HOSO-7, E = - eV

Figure S26: Molecular orbitals for **Rc-Ru**^{acac} in its neutral and oxidized states.

neutral state	oxidized state	
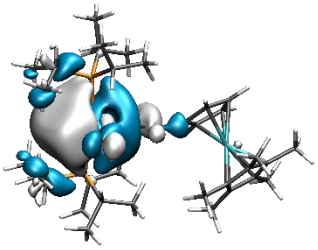	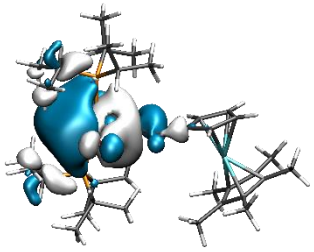	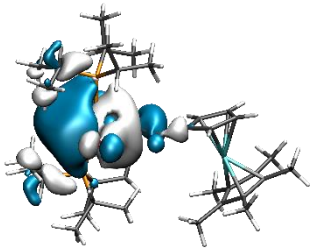
LUMO, E = -1.43 eV	α-LUSO, E = -2.21 eV	β-LUSO+1, E = -2.16 eV
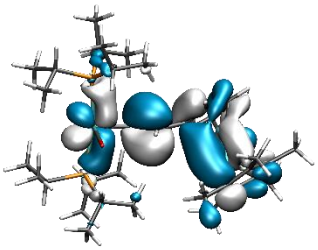	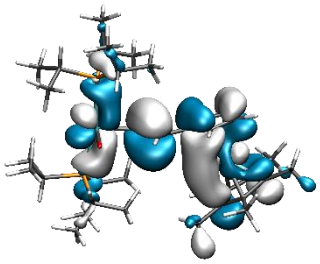	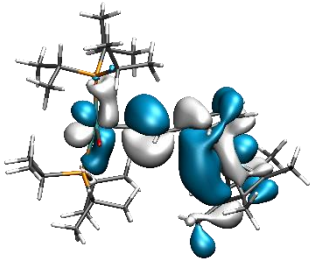
HOMO, E = -5.03 eV	α-HOSO, E = - 5.92eV	β-LUSO, E = -3.94 eV
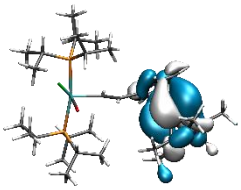		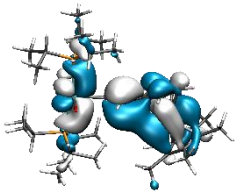
HOMO-1, E = -5.54 eV		β-HOSO, E = -6.37 eV
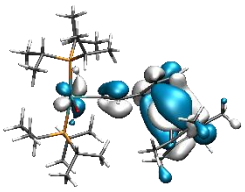		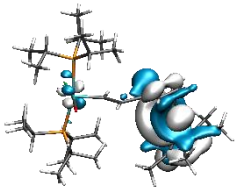
HOMO-2, E = -5.61 eV		β-HOSO-1, E = -6.73 eV
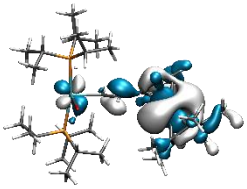		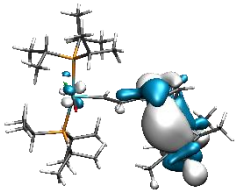
HOMO-3, E = -5.79 eV		β-HOSO-2, E = -6.76 eV

Figure S27: Molecular orbitals for **Rc*-Ru^{Cl}** in its neutral and oxidized states.

neutral state	oxidized state	
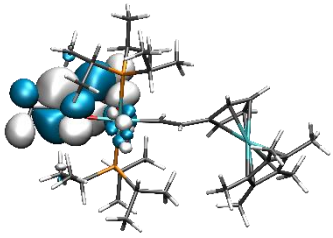 LUMO, E = -0-77 eV	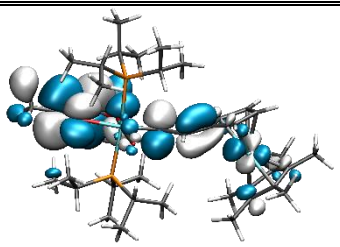 α-LUSO, E = --1-19 eV	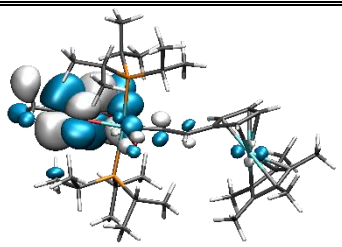 β-LUSO+1, E = -1.16 eV
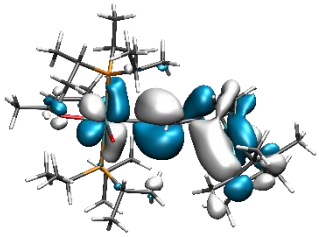 HOMO, E = -4.88eV	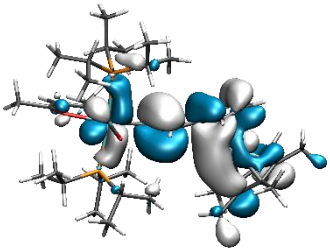 α-HOSO, E = -5.78 eV	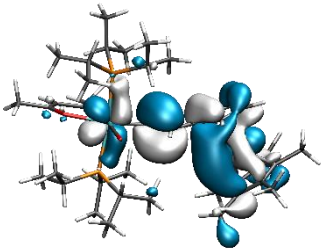 β-LUSO, E = -3.82 eV
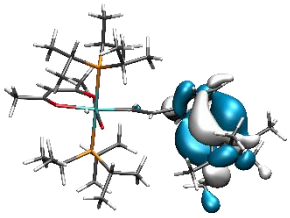 HOMO-1, E = -5.47 eV		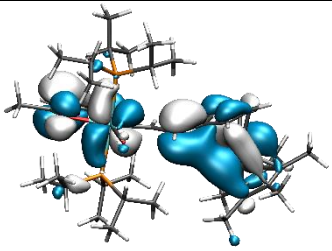 β-HOSO, E = -6.15 eV
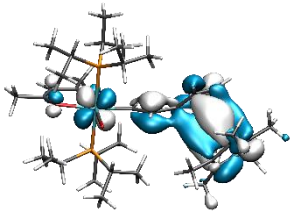 HOMO-2, E = -5.50 eV		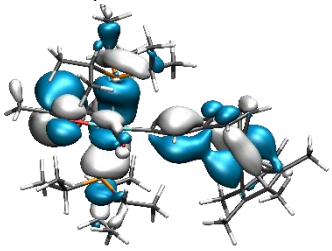 β-HOSO-1, E = -6.32 eV
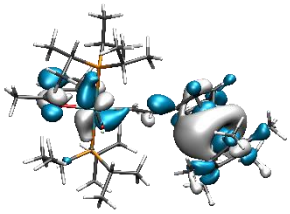 HOMO-3, E = -5.68 eV	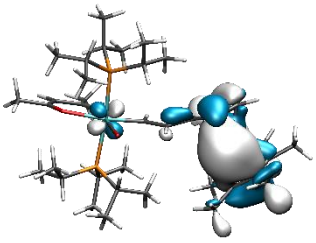 β-HOSO-3, E = -6.59 eV	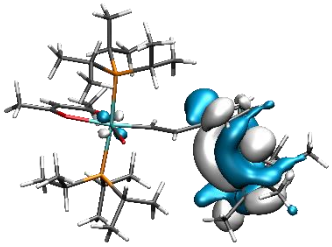 β-HOSO-2, E = -6.59 eV

Figure S28: Molecular orbitals for **Rc*-Ru^{acac}** in its neutral and oxidized states.

neutral state	oxidized state	
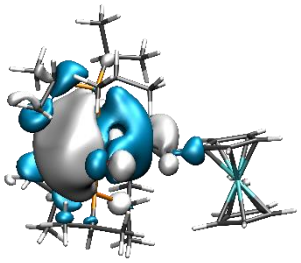	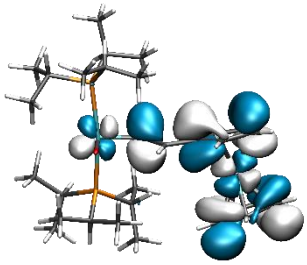	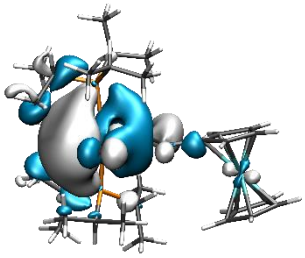
LUMO, E = -1.53 eV	α-LUSO, E = -1.19 eV	β-LUSO+1, E = -2.39 eV
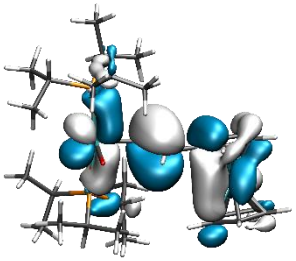	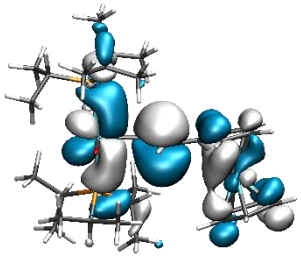	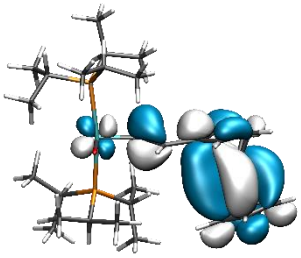
HOMO, E = -5.27 eV	α-HOSO, E = -5.78 eV	β-LUSO, E = -2.73 eV
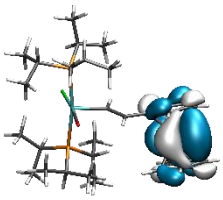	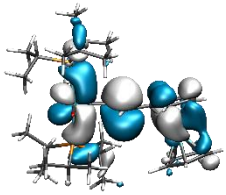	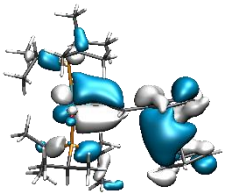
HOMO-1, E = -5.77 eV	β–HOSO, E = -6.24 eV	β–HOSO-4, E = -8.12 eV
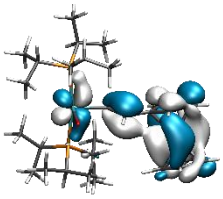	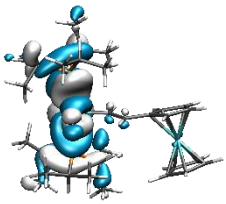	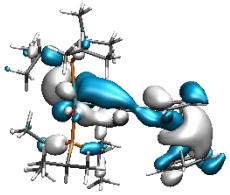
HOMO-2, E = -5.88 eV	β–HOSO-1, E = -6.90 eV	β–HOSO-5, E = -8.28 eV
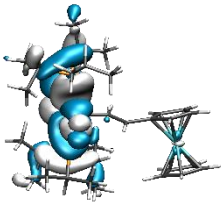	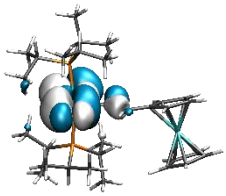	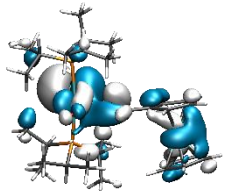
HOMO-3, E = -6.50 eV	β–HOSO-2, E = -7.13 eV	β–HOSO-6, E = -8.35 eV

Figure S29: Molecular orbitals for **Fc-Ru^{Cl}** in its neutral and oxidized states.

neutral state	oxidized state	
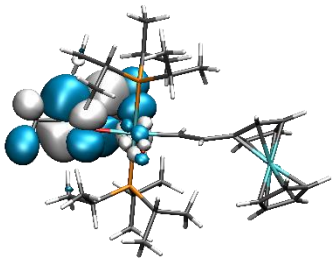 LUMO, E = -0.91 eV	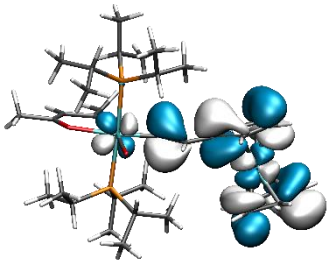 α-LUSO, E = -2.66 eV	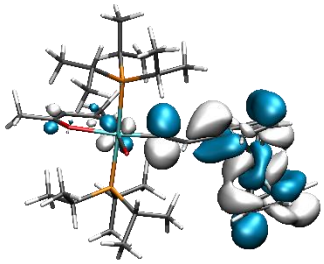 β-LUSO+1, E = -1.56 eV
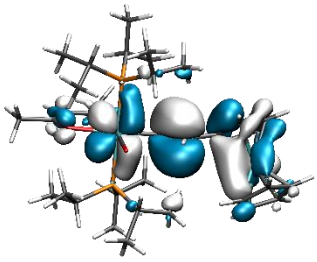 HOMO, E = -5.09 eV	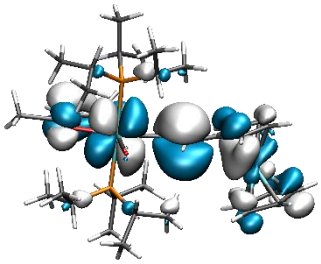 α-HOSO, E = -5.99 eV	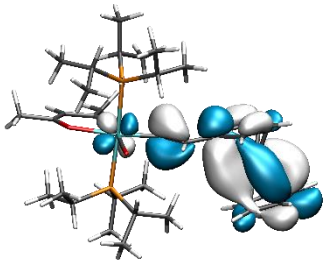 β-LUSO, E = -3.10 eV
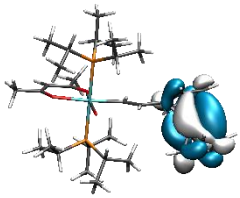 HOMO-1, E = -5.68 eV	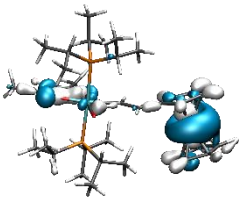 α–HOSO-14, E = -8.86 eV	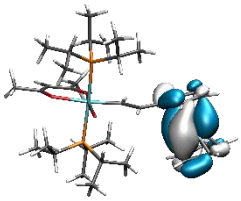 β–HOSO-8, E = -8.17 eV
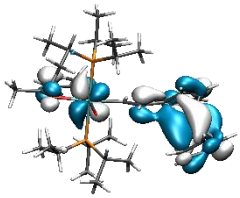 HOMO-2, E = -5.74 eV	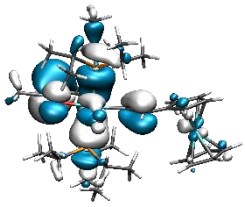 α–HOSO-1, E = -6.28 eV	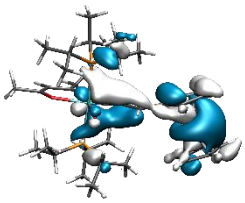 β–HOSO-7, E = -8.06 eV
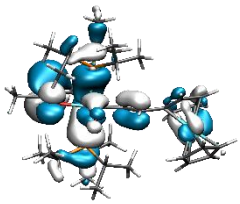 HOMO-3, E = -5.95 eV		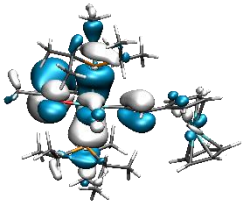 β–HOSO-1, E = -6.28 eV

Figure S30: Molecular orbitals for **Fc-Ru**^{acac} in its neutral and oxidized states.

Table S5. Fragment contributions to the charge and spin densities according to analysis of the natural bond orbitals

complex	fragment	n = 0	n = 1		charge difference
		charge	charge	spin density	
Fc-Ru^{Cl}	{Ru^{Cl}}	0.10	0.12	0.01	0.02
	vinyl	-0.03	0.02	0.01	0.05
	Cp$^{vi\ a)}$	0.05	0.05	-0.12	0.00
	Fe	-0.21	0.72	1.29	0.93
	Cp$^{b)}$	0.09	0.09	-0.19	0.00
	SUM	0.00	1.00	1.00	1.00
Fc-Ru^{acac}	{Ru^{acac}}	0.24	0.19	0.00	-0.05
	vinyl	-0.15	-0.03	0.01	0.12
	Cp$^{vi\ a)}$	0.03	0.03	-0.19	0.00
	Fe	-0.20	0.73	1.30	0.93
	Cp $^{b)}$	0.08	0.08	-0.12	0.00
	SUM	0.00	1.00	1.00	1.00
Rc-Ru^{Cl}	{Ru^{Cl}}	0.10	0.35	0.28	0.25
	vinyl	-0.02	0.25	0.30	0.27
	Cp$^{vi\ a)}$	0.09	0.15	0.04	0.06
	Ru	-0.31	0.07	0.33	0.38
	Cp $^{b)}$	0.14	0.18	0.05	0.04
	SUM	0.00	1.00	1.00	1.00
Rc-Ru^{acac}	{Ru^{acac}}	0.23	0.47	0.23	0.24
	vinyl	-0.13	0.23	0.36	0.36
	Cp$^{vi\ a)}$	0.08	0.13	0.05	0.05
	Ru	-0.31	0.01	0.33	0.32
	Cp $^{b)}$	0.13	0.16	0.03	0.03
	SUM	0.00	1.00	1.00	1.00
Rc*-Ru^{Cl}	{Ru^{Cl}}	0.09	0.25	0.18	0.16
	vinyl	-0.02	0.18	0.23	0.20
	Cp$^{vi\ a)}$	0.02	0.15	0.07	0.13
	Ru	-0.26	0.18	0.45	0.44
	Cp* $^{b)}$	0.17	0.24	0.07	0.07
	SUM	0.00	1.00	1.00	1.00
Rc*-Ru^{acac}	{Ru^{acac}}	0.23	0.34	0.21	0.11
	vinyl	-0.13	0.18	0.28	0.31
	Cp$^{vi\ a)}$	0.02	0.13	0.07	0.11
	Ru	-0.26	0.13	0.38	0.39
	Cp* $^{b)}$	0.14	0.22	0.07	0.08
	SUM	0.00	1.00	1.00	1.00

^{a}The bridging, vinyl substituted Cp ligand. ^{b}The appended, non-bridging Cp/Cp* ligand.

7. EPR spectra of the chemically mono-oxidized complexes

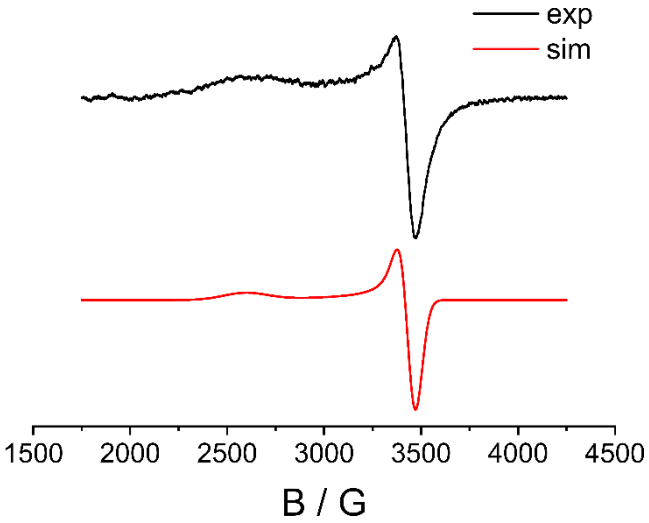

Figure S31: EPR spectra of **Fc-Ru**$^{acac+}$ at -150°C in a frozen dichloromethane matrix.

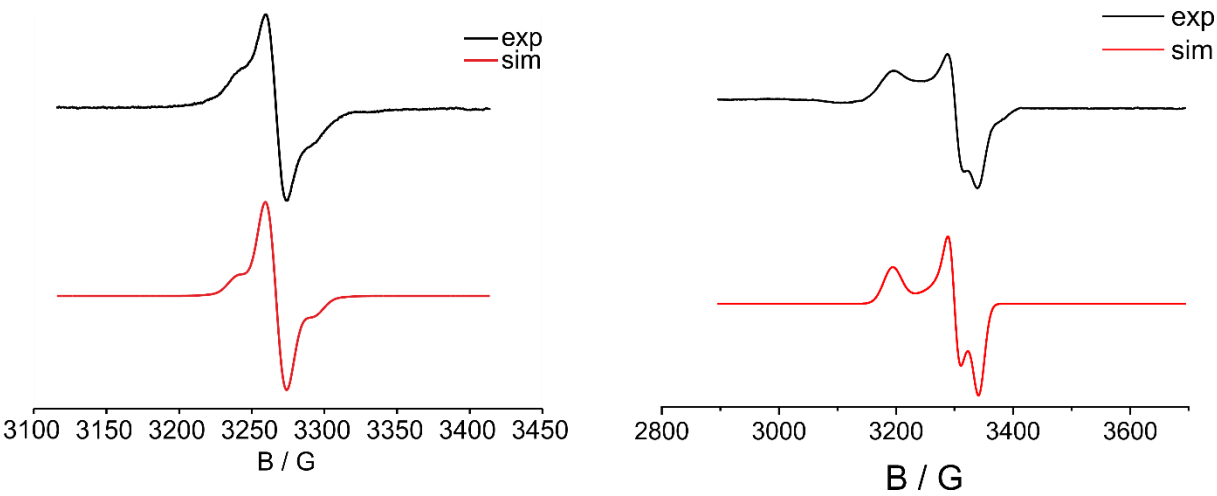

Figure S32: EPR spectra of **Rc-Ru**$^{acac+}$ at room temperature (left) and at -150°C in a frozen dichloromethane matrix (right).

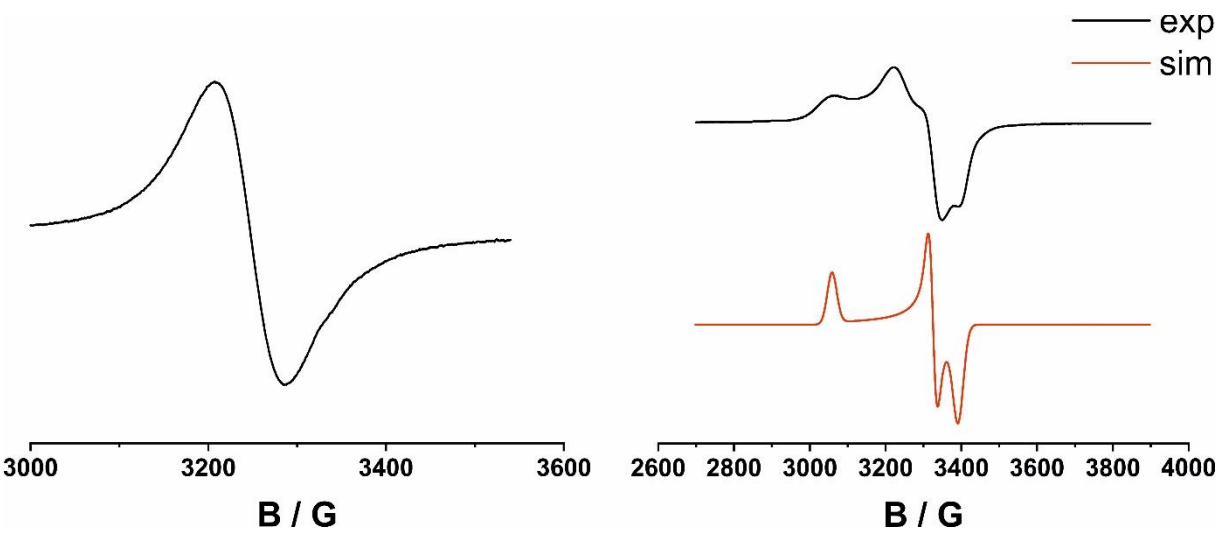

Figure S33: EPR spectra of **Rc*-Ru**$^{Cl+}$ at room temperature (left) and at -150°C in a frozen dichloromethane matrix (right).

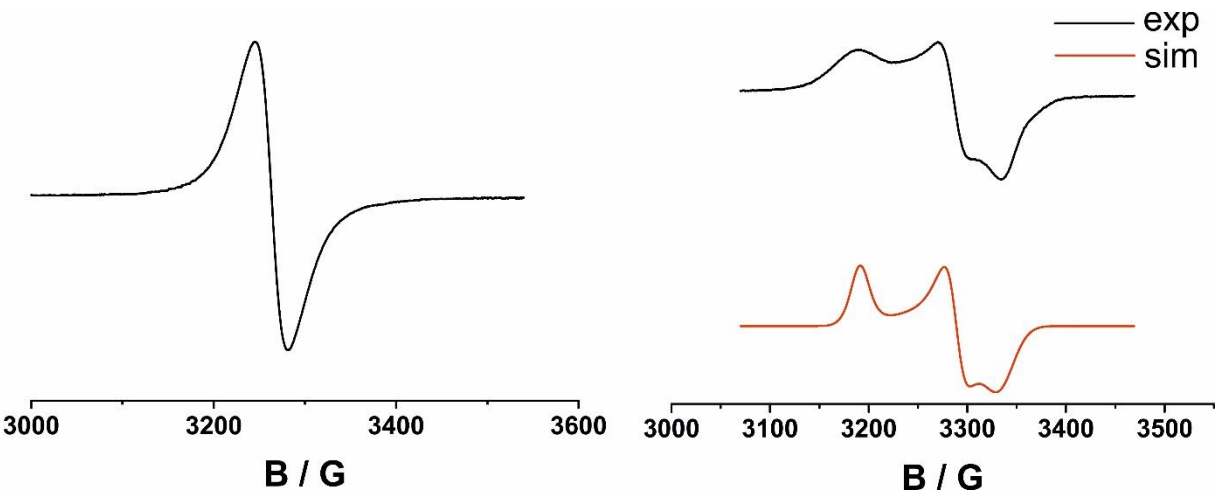

Figure S34: EPR spectra of **Rc*-Ru**$^{acac+}$ at room temperature (left) and at -150°C in a frozen dichloromethane matrix (right).

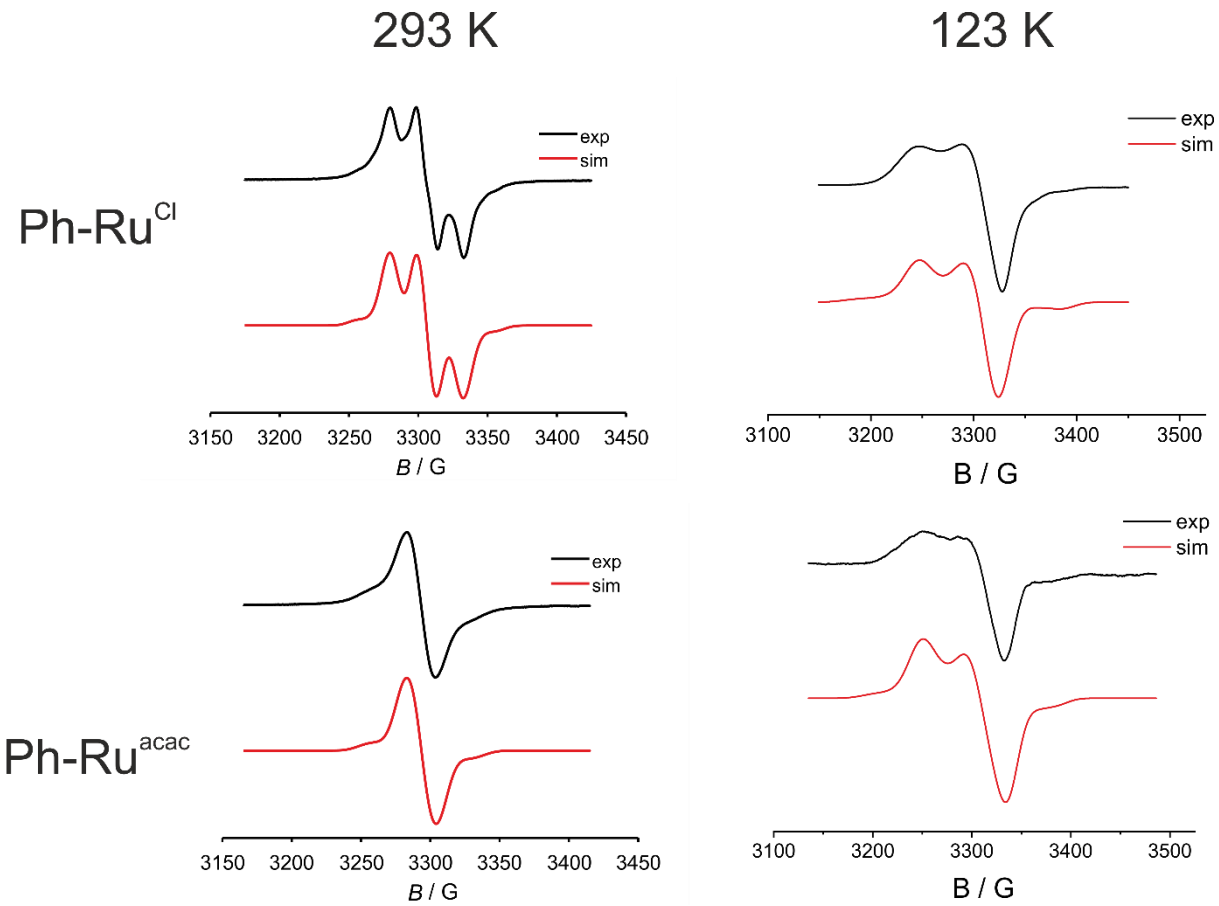

Figure S35: EPR spectra of **Ph-Ru**$^{Cl+}$and **Ph-Ru**$^{acac+}$ at room temperature (left) and at -150°C in a frozen dichloromethane matrix (right).

8. Spin Density Plots of the radical cations

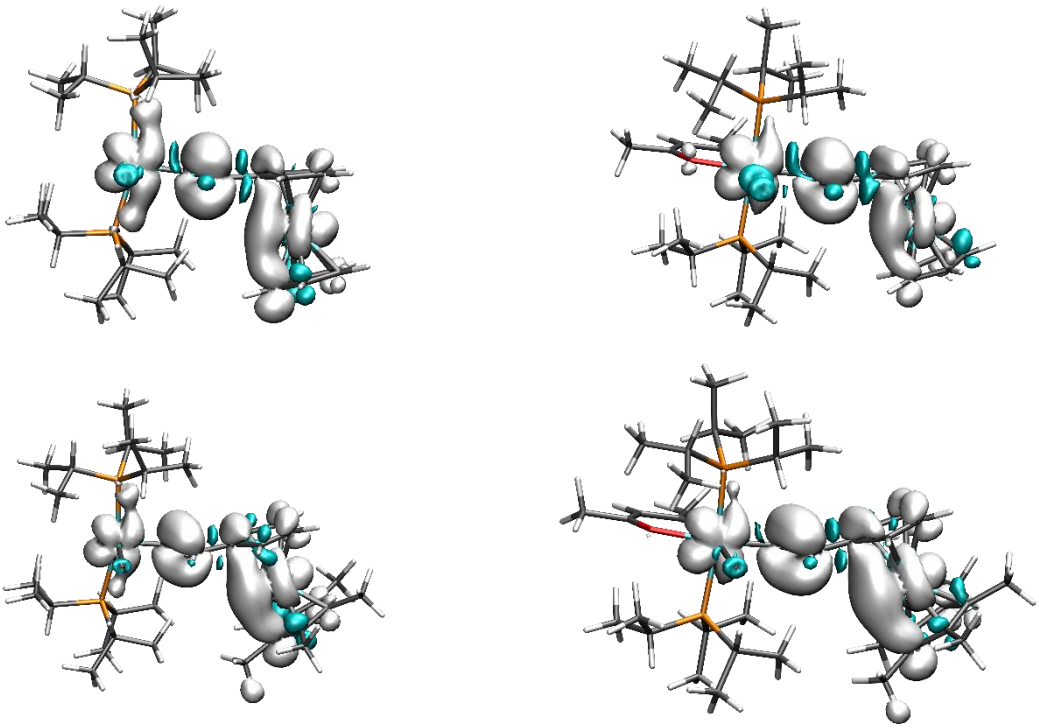

Figure S36: Spin density plots of **Rc-Ru^{Cl}** (upper left), **Rc-Ru^{acac}** (upper right), **Rc*-Ru^{Cl}** (bottom left), **Rc*-Ru^{acac}** (bottom right), white and cyan color positive (α) and negative (β) spin density, respectively (pbe1pbe/6-31G(d) level of theory).

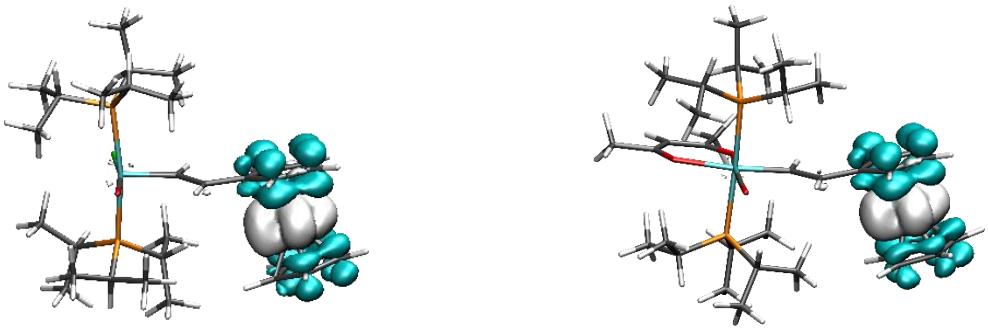

Figure S37: Spin density plots of **FcRu^{Cl}** (left), **Fc-Ru^{acac}** (right), white and cyan color positive (α) and negative (β) spin density, respectively (pbe1pbe/6-311G(d) level of theory).

Table S6. DFT-computed fragment contributions to the β-MOs relevant to the NIR band of the radical cations

		%[a]	Mc[b]	Cp[c]	vinyl	Ru[d]
Fc-Ru^{Cl+}	LUSO		37	50	9	4
	HOSO	56	7	16	31	46
	HOSO-1	22	0	0	2	98
Fc-Ru^{acac+}	LUSO		65	23	8	4
	HOSO	63	8	13	26	53
	HOSO-1	19	1	3	5	91
Rc-Ru^{Cl+}	LUSO		26	19	29	26
	HOSO	56	52	16	10	22
	HOSO-1	22	73	17	1	9
Rc-Ru^{acac+}	LUSO		20	16	32	32
	HOSO	61	22	6	2	70
	HOSO-1	24	42	12	4	42
Rc*-Ru^{Cl+}	LUSO		36	25	22	17
	HOSO	77	38	15	15	32
	HOSO-1	11	64	31	1	4
Rc*-Ru^{acac+}	LUSO		29	25	26	20
	HOSO	58	28	11	8	53
	HOSO-3	24	71	25	1	3

[a]Percent contribution of corresponding excitation. [b]Contribution of the Fe or Ru atom of the metallocene. [c]Combined contributions of the cyclopentadienyl ligands [d]Contribution of the Ru(CO)(L)(P^iPr_3)$_2$ (L = Cl^- or $acac^-$) entity.

9. UV/vis/NIR data

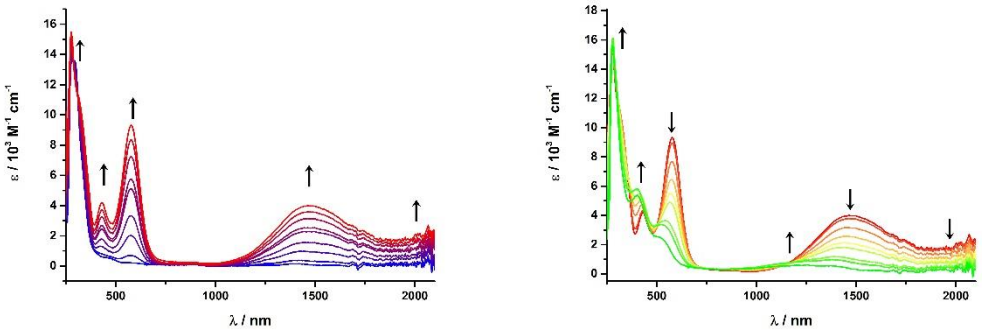

Figure S38: UV/vis/NIR spectroelectrochemistry during oxidation of **Fc-Ru^{acac}** in dichloromethane and NBu_4PF_6 as supporting electrolyte (0.1 M) at room temperature, blue neutral, red cationic and green dicationic form.

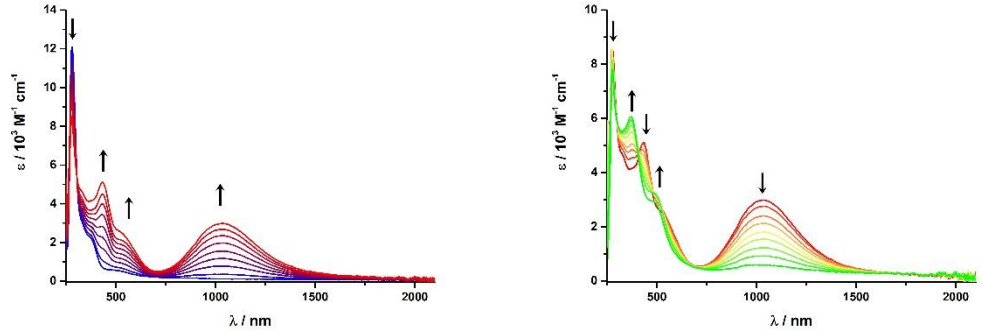

Figure S39: UV/vis/NIR spectroelectrochemistry during oxidation of **Rc-Ru^{Cl}** in dichloromethane and NBu_4PF_6 as supporting electrolyte (0.1 M) at room temperature, blue neutral, red cationic and green dicationic form.

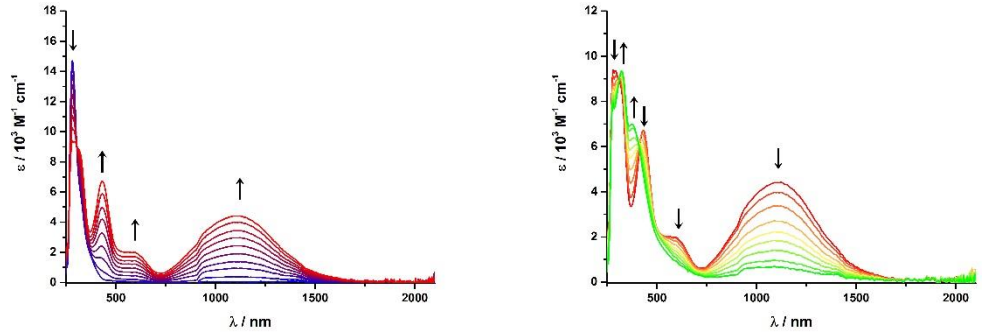

Figure S40: UV/vis/NIR spectroelectrochemistry during oxidation of **Rc-Ru^{acac}** in dichloromethane and NBu_4PF_6 as supporting electrolyte (0.1 M) at room temperature, blue neutral, red cationic and green dicationic form.

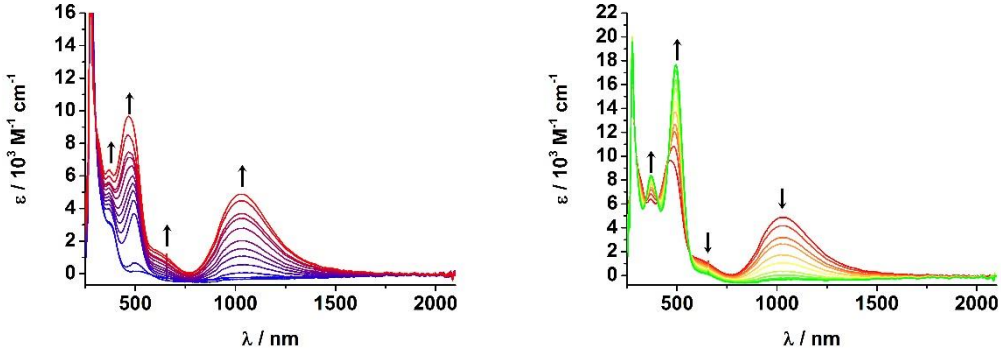

Figure S41: UV/vis/NIR spectroelectrochemistry during oxidation of **Rc*-Ru^{Cl}** in dichloromethane and NBu_4PF_6 as supporting electrolyte (0.1 M) at room temperature, blue neutral, red cationic and green dicationic form.

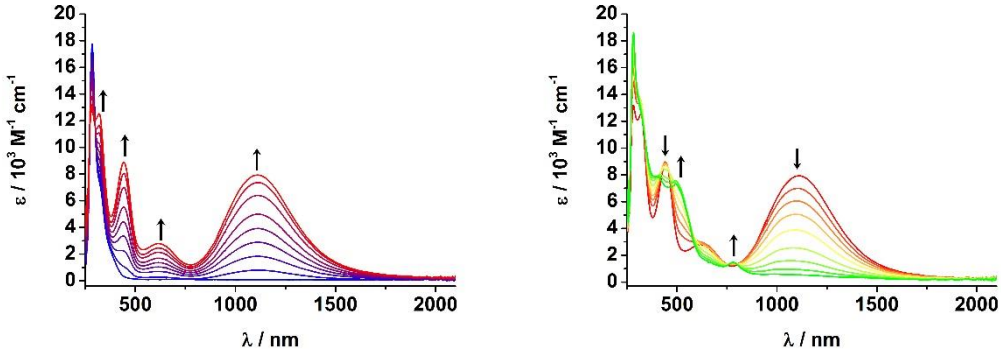

Figure S42: UV/vis/NIR spectroelectrochemistry during oxidation of **Rc*-Ru^{acac}** in dichloromethane and NBu_4PF_6 as supporting electrolyte (0.1 M) at room temperature, blue neutral, red cationic and green dicationic form.

10. TD-DFT calculated UV/vis/NIR spectra

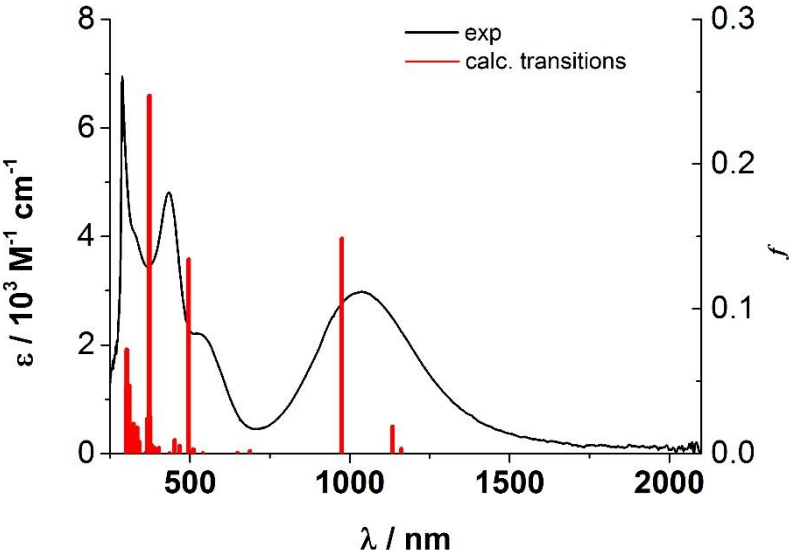

Figure S43: TD-DFT calculated transitions of **Rc-Ru^{Cl+}** (pbe1pbe/6-31G(d) level of theory)

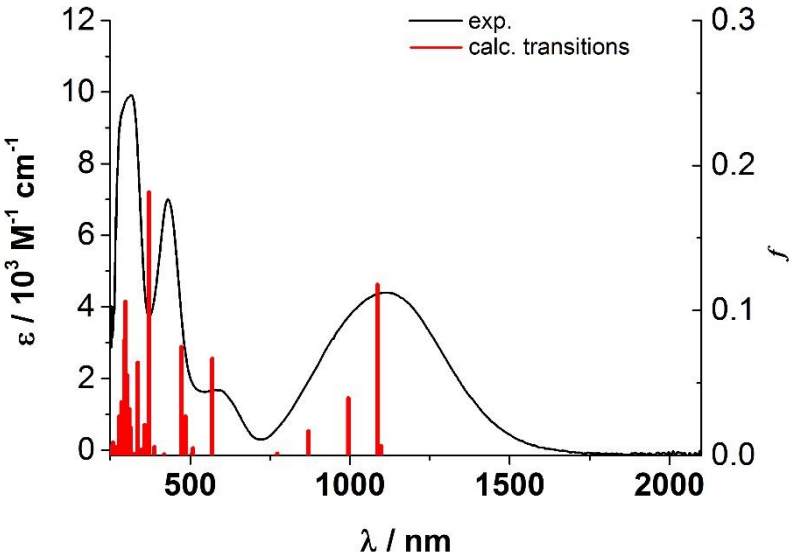

Figure S44: TD-DFT calculated transitions of **Rc-Ru^{acac+}** c (pbe1pbe/6-31G(d) level of theory)

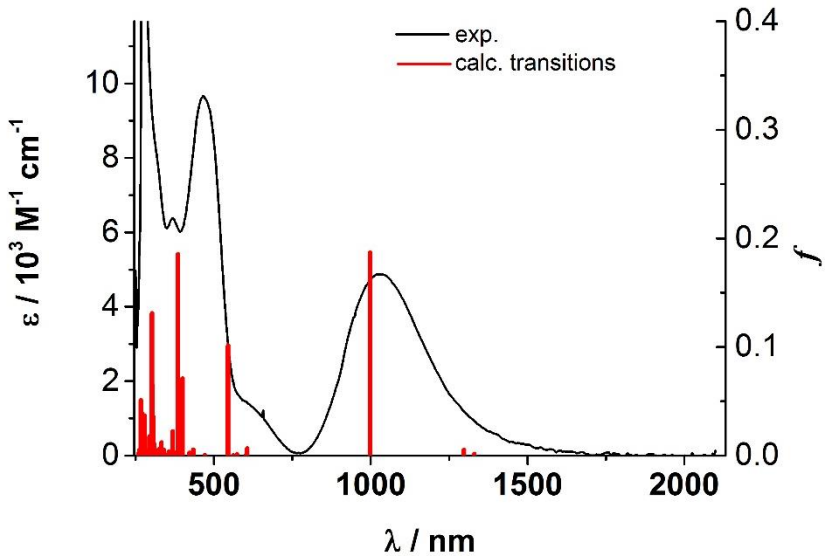

Figure S45: TD-DFT calculated transitions of **Rc*-Ru^{Cl+}** (pbe1pbe/6-31G(d) level of theory)

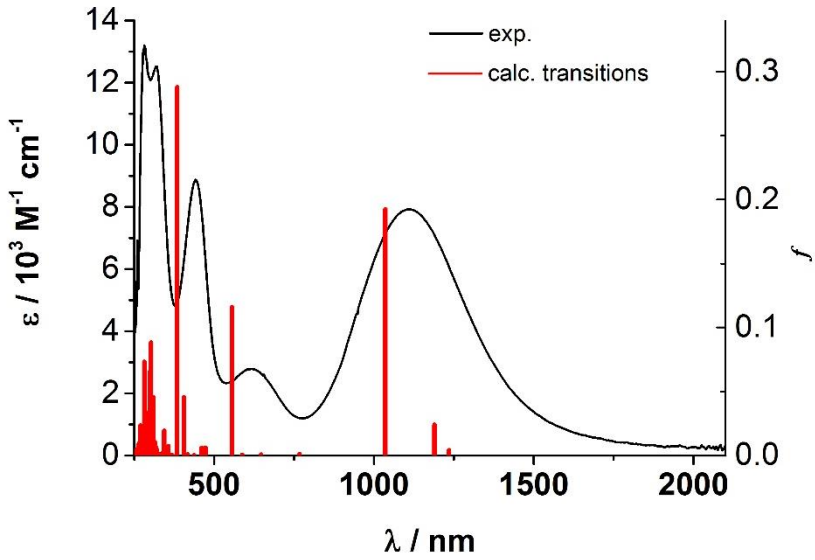

Figure S46: TD-DFT calculated transitions of **Rc*-Ru^{acac+}** (pbe1pbe/6-31G(d) level of theory)

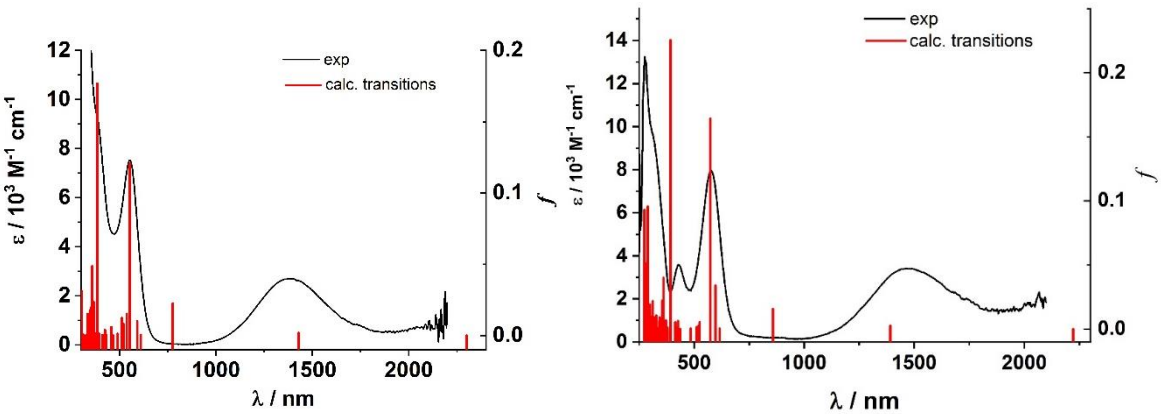

Figure S47: TD-DFT calculated transitions of **Fc-Ru^{Cl+}** (left) and **Fc-Ru^{acac+} (right)** (pbe1pbe/6-311G(d) level of theory)

11. Electron Density Difference Maps (EDDM) for the calculated transitions

Table S7. Selected calculated transition energies for **Fc-Ru^{Cl+}**.

transition number	calc. λ_{max}	major transition	oscillator strength
1	2299	HOSO-7(β)->LUSO(β) (86 %),	0.0
2	1428	HOSO-6(β) → LUSO(β) (10%) HOSO-5(β) → LUSO(β) (30%) HOSO-4(β) → LUSO(β) (46%)	0.0019
3	776	HOSO-2(β) → LUSO(β) (11%) HOSO-1(β) → LUSO(β) (22%) HOSO(β) → LUSO(β) (56%)	0.0227
6	554	HOSO-6(β) → LUSO(β) (83%)	0.1208
18	385	HOSO-19(α) → LUSO(α) (10%) HOSO(α) → LUSO(α) (14%), HOSO(β) → LUSO+2(β) (47%)	0.1769

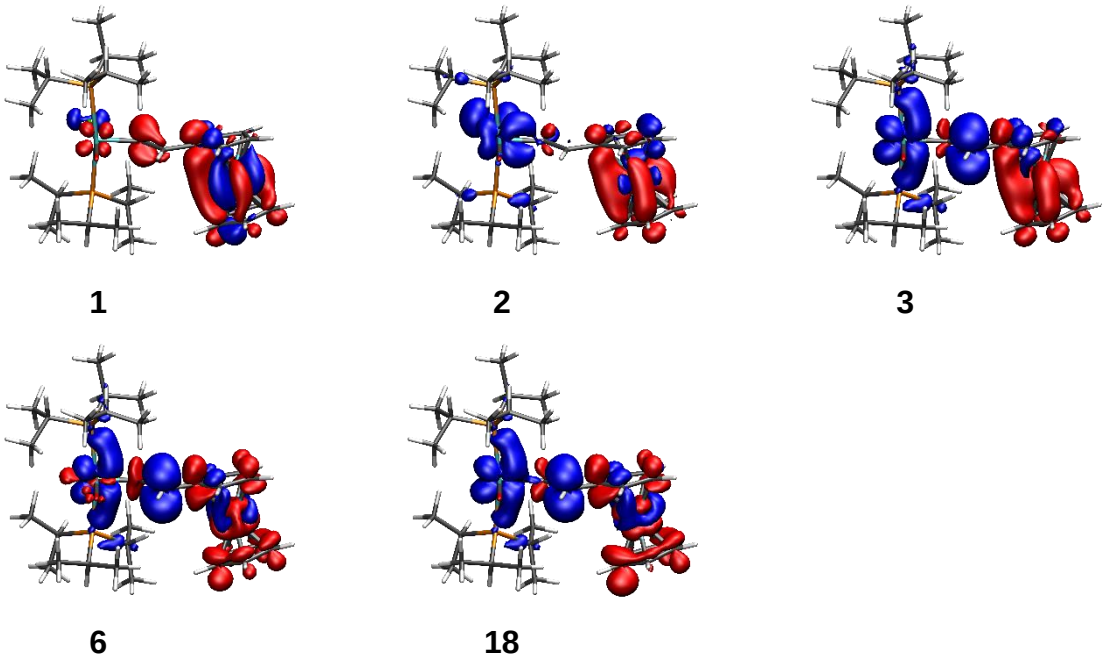

Figure S48: Electron density difference map for the selected transitions of **Fc-Ru^{Cl}**. Blue color indicates a decreasing and red color indicates an increasing electron density during the respective excitation.

Table S8. Selected calculated transition energies for **Fc-Ru^{acac+}**.

transition number	calc. λ_{max}	major transition	oscillator strength
1	2222	HOSO-8(β) → LUSO(β) (89 %),	0.0
2	1392	HOSO-7(β) → LUSO(β) (53%) HOSO-6(β) → LUSO(β) (29%)	0.0024
3	857	HOSO(β) → LUSO(β) (63%) HOSO-1(β) → LUSO(β) (19%)	0.0157
6	574	HOSO(α) → LUSO(α) (41%) HOSO-7(β) → LUSO+1(β) (38%) HOSO-6(β) → LUSO+2(β) (21%)	0.1642
16	393	HOSO-1(α) → LUSO(α) (47%)	0.2254

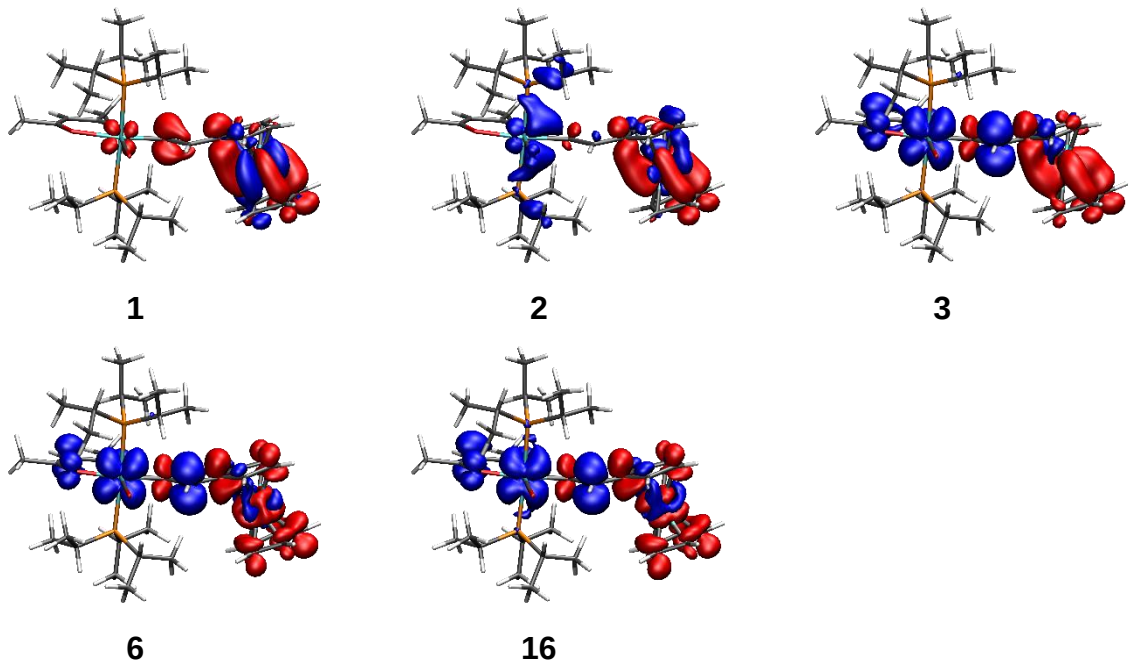

Figure S49: Electron density difference map for the selected transitions of **Fc-Ru^{acac+}**. Blue color indicates a decreasing and red color indicates an increasing electron density during the respective excitation.

Table S9. Selected calculated transition energies for **Rc-Ru^{Cl+}**.

transition number	calc. λ_{max}	major transition	oscillator strength
1	1160	HOSO-2(β) → LUSO(β) (31%) HOSO -1(β) → LUSO(β) (58%)	0.0031
2	1134	HOSO-2(β) → LUSO(β) (53%) HOSO-1(β) → LUSO(β) (11%) HOSO(β) → LUSO(β) (32%)	0.0186
3	975	HOSO-2(β) → LUSO(β) (11%) HOSO-1(β) → LUSO(β) (22%) HOSO(β) → LUSO(β) (56%)	0.1485
8	496	HOSO-6(β) → LUSO(β) (83%)	0.1342
16	373	HOSO(α) → L+1(α) (61%)	0.2472

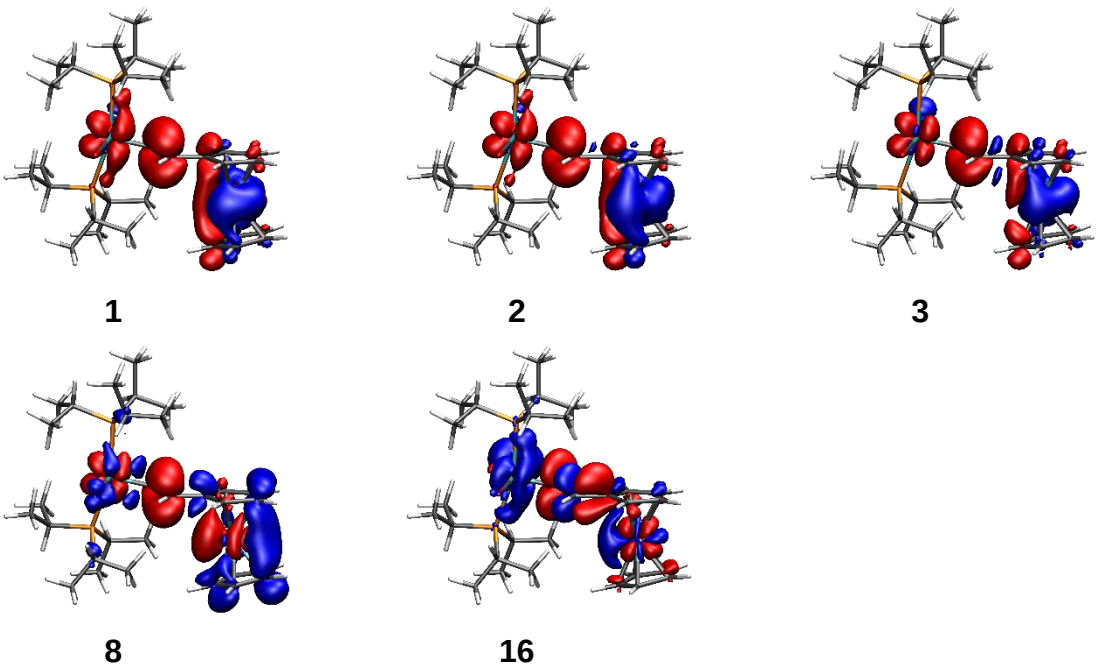

Figure S50: Electron density difference map for the selected transitions of **Rc-Ru^{Cl}**. Blue color indicates a decreasing and red color indicates an increasing electron density during the respective excitation.

Table S10. Selected calculated transition energies for **Rc-Ru^{acac+}**.

transition number	calc. λ_{max}	major transition	oscillator strength
1	1097	HOSO-2(β) → LUSO(β) (90%)	0.0064
2	1086	HOSO-1(β) → LUSO(β) (24%) HOSO(β) → LUSO(β) (61%)	0.1178
3	995	HOSO-3(β) → LUSO(β) (69%) HOSO(β) → LUSO(β) (18%)	0.0394
4	870	HOSO-3(β) → LUSO(β) (20%) HOSO-1(β) → LUSO(β) (59%), HOSO(β) → LUSO(β) (12%)	0.0165
6	569	HOSO-7(β) → LUSO(β) (32%), HOSO-5(β) → LUSO(β) (50%)	0.0666
10	473	HOSO-9(β) → LUSO(β) (38%) HOSO-8(β) → LUSO(β) (25%) HOSO-7(β) → LUSO(β) (23%) HOSO-5(β) → LUSO(β) (10%)	0.0748
13	371	HOSO(α) → L+1(α) (48%)	0.1815

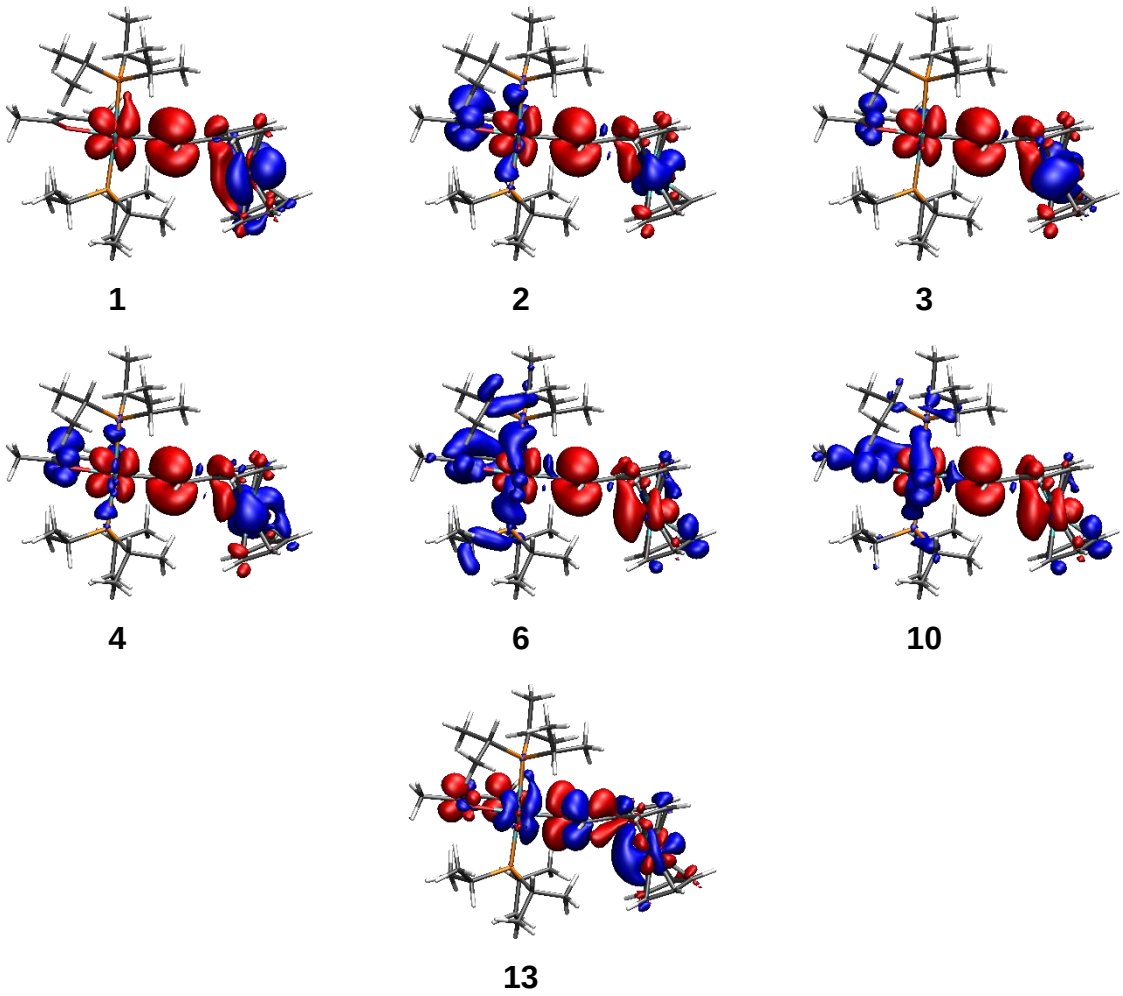

Figure S51: Electron density difference map for the selected transitions of **Rc-Ru^{acac}**. Blue color indicates a decreasing and red color indicates an increasing electron density during the respective excitation.

Table S11. Selected calculated transition energies for **Rc*-Ru^{Cl+}**.

transition number	calc. λ_{max}	major transition	oscillator strength
1	1331	HOSO-1(β)→LUSO(β) (84%)	0.0015
2	1298	HOSO-2(β)→LUSO(β) (77%), HOSO(β)→LUSO(β) (13%)	0.0054
3	998	HOSO(β)→LUSO(β) (77%)	0.187
8	545	HOSO-6(β)→LUSO(β) (90%)	0.1012
14	386	HOSO(α)→LUSO+1(α) (55%), HOSO-3(β)→LUSO+1(β) (11%)	0.1854

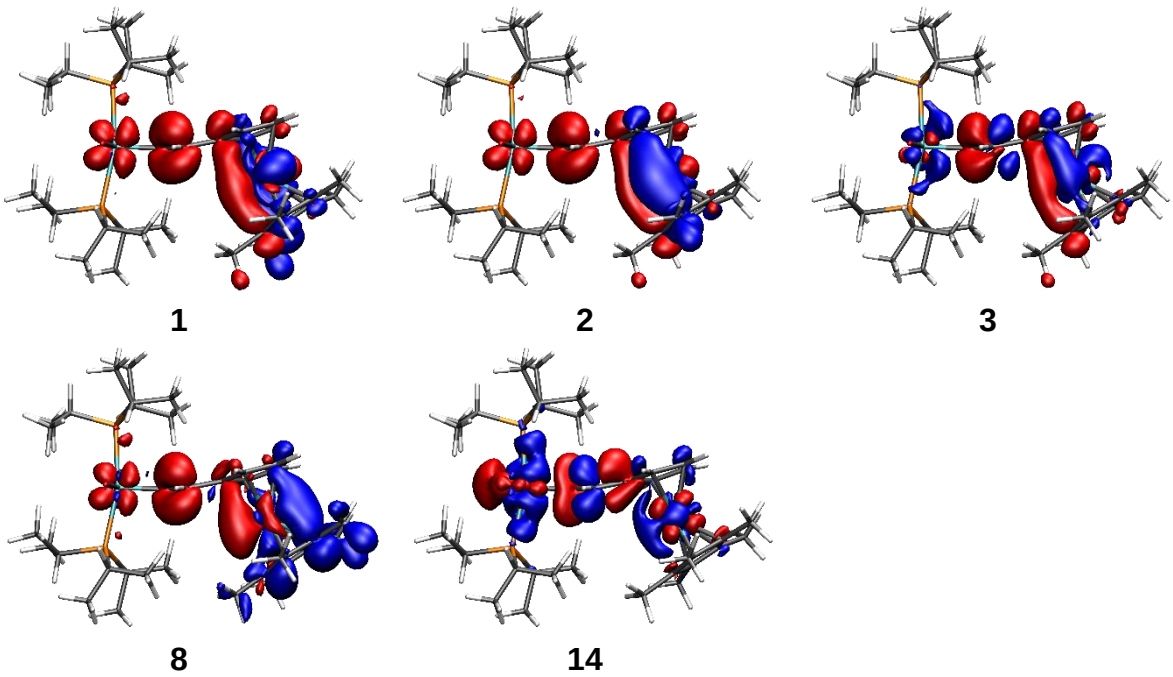

Figure S52: Electron density difference map for the selected transitions of **Rc*-Ru^{Cl}**. Blue color indicates a decreasing and red color indicates an increasing electron density during the respective excitation.

Table S12. Selected calculated transition energies for **Rc*-Ru^{acac+}**.

transition number	calc. λ_{max}	major transition	oscillator strength
1	1234	HOSO-2(β)→LUSO(β) (87%)	0.0042
2	1189	HOSO-3(β)→LUSO(β) (68%), HOSO-1(β)→LUSO(β) (10%), HOSO(β)→LUSO(β) (17%)	0.024
3	1036	HOSO-3(β)->LUSO(β) (24%), HOSO(β)→LUSO(β) (58%)	0.1925
7	556	HOSO-6(β)→LUSO(β) (87%)	0.1159
13	384	HOSO(α)→LUSO(α) (21%), HOSO(α)→LUSO+1(α) (57%)	0.2881

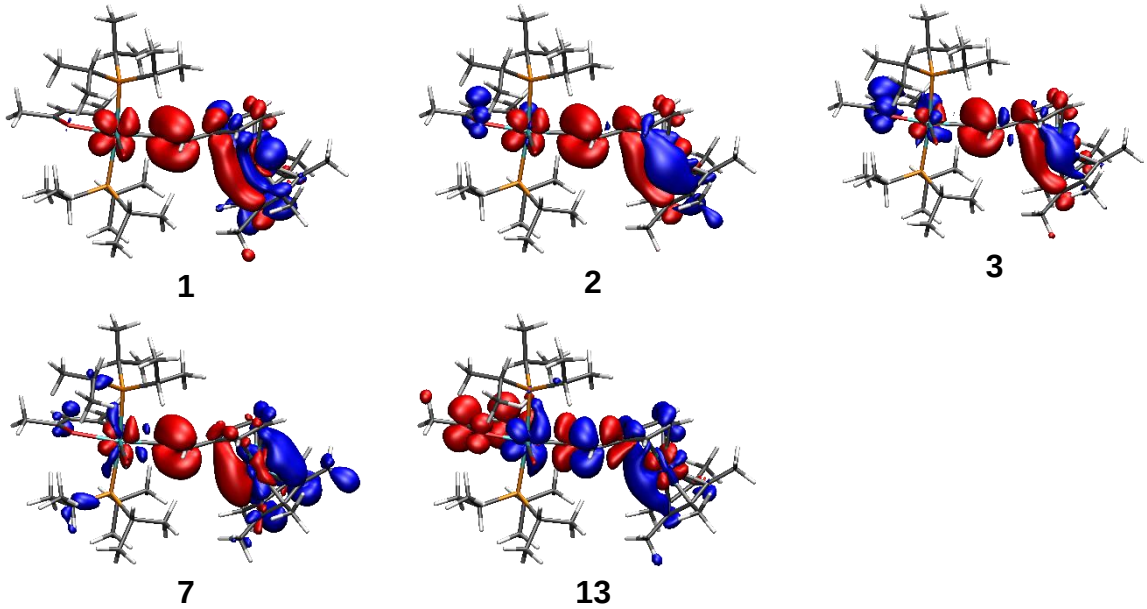

Figure S53: Electron density difference map for the selected transitions of **Rc*-Ru^{acac}**. Blue color indicates decreasing and red color increasing electron density during the respective excitation.

12. Molecular orbital contributions

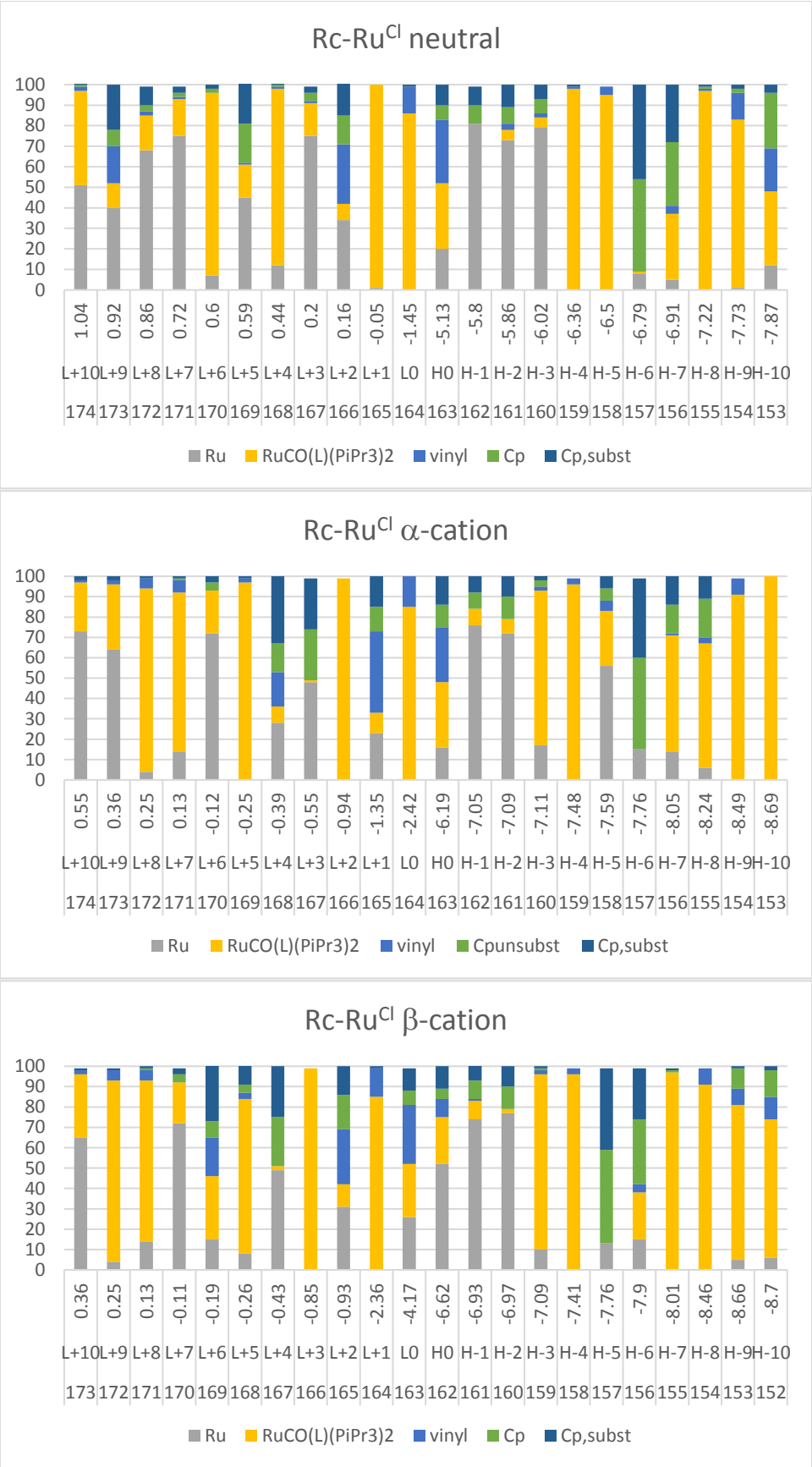

Figure S54: Fragment contributions to the frontier MOs in **Rc-Ru^{Cl}** and **Rc-Ru^{Cl+}**

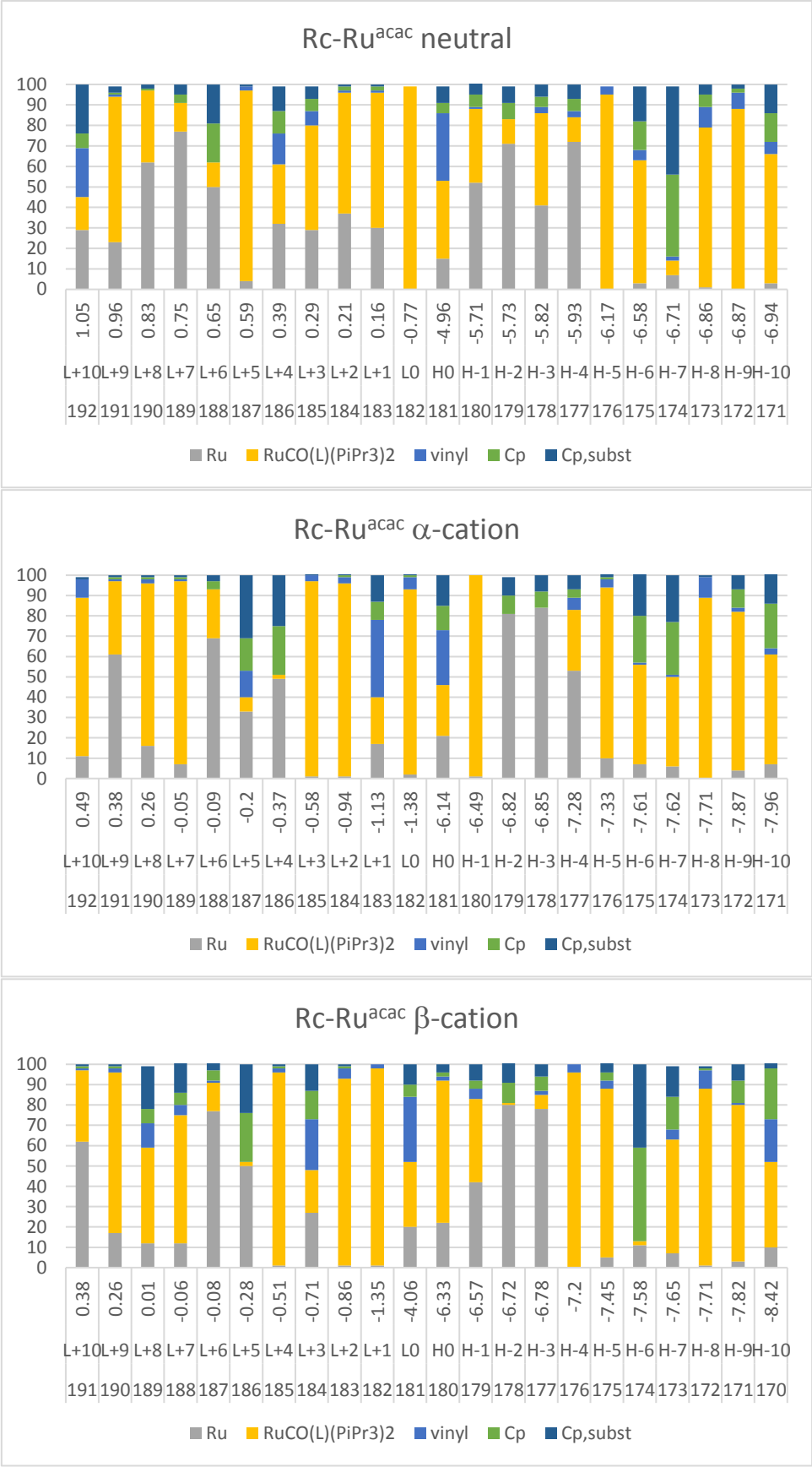

Figure S55: Fragment contributions to the frontier MOs in **Rc-Ru^{acac}** and **Rc-Ru$^{acac\ +}$**

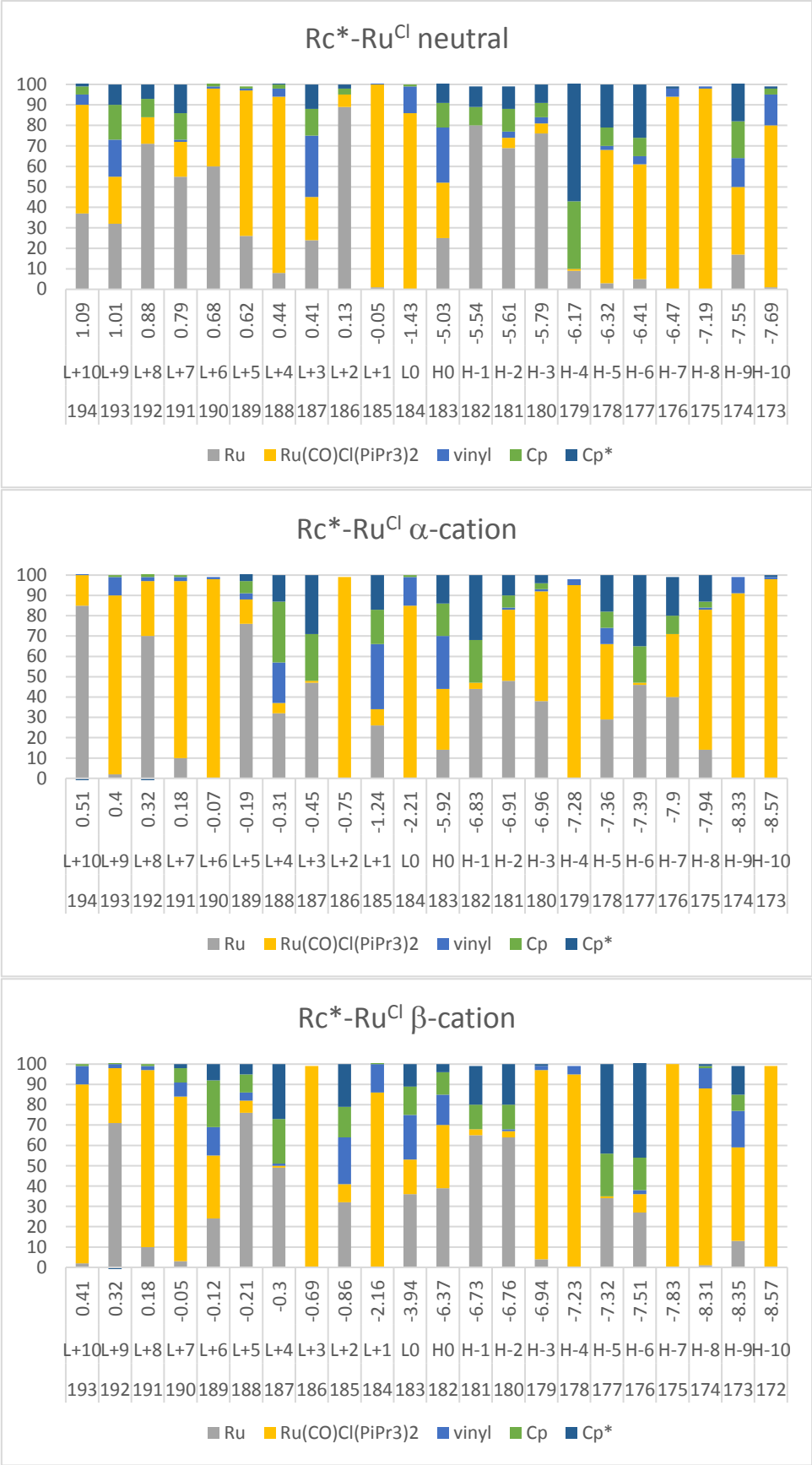

Figure S56: Fragment contributions to the frontier MOs in **Rc*-Ru^{Cl}** and **Rc*-Ru$^{Cl\,+}$**

Figure S57: Fragment contributions to the frontier MOs in **Rc*-Ru^{acac}** and **Rc*-Ru$^{acac\ +}$**

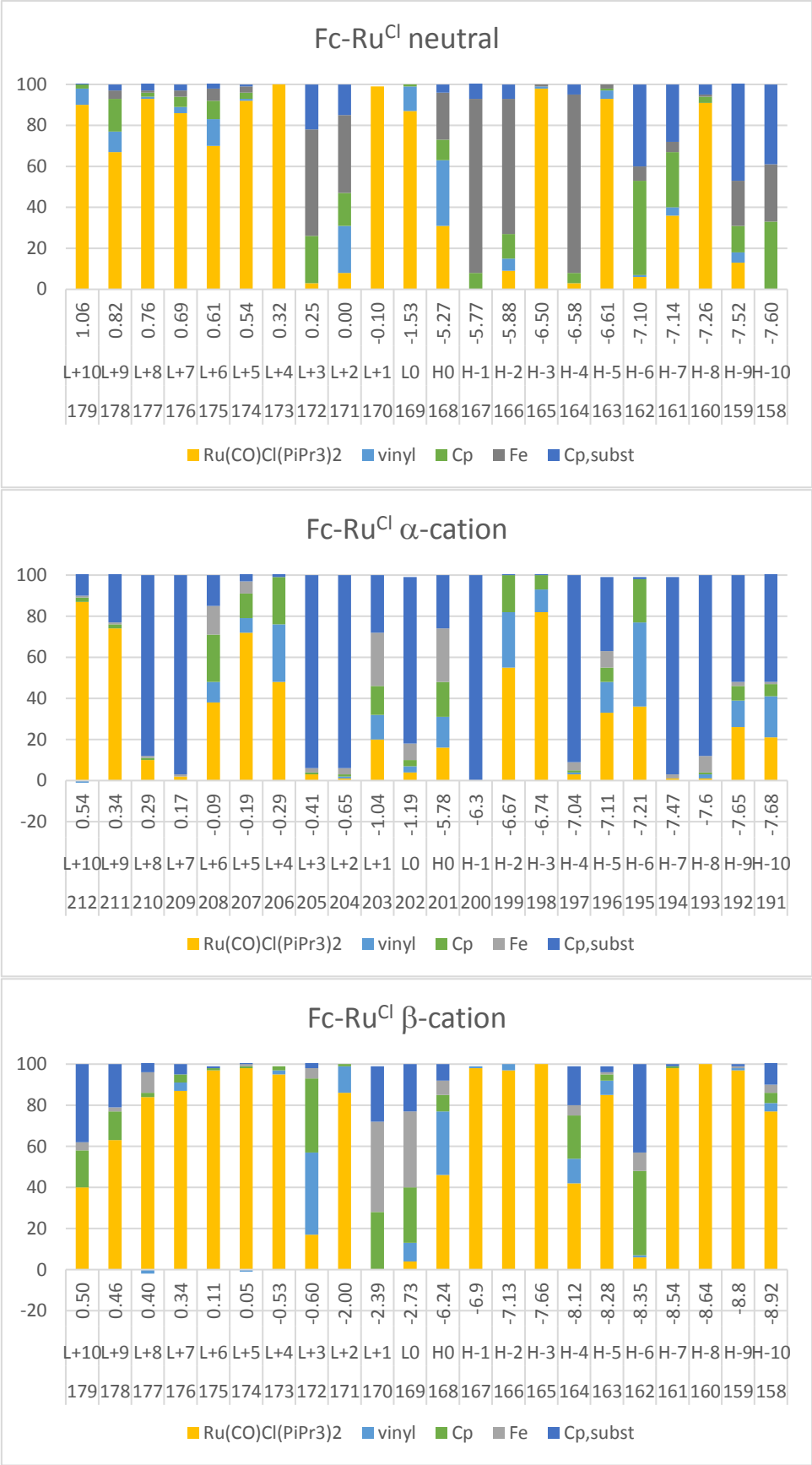

Figure S58: Fragment contributions to the frontier MOs in **Fc-Ru^{Cl}** and **Fc-Ru^{Cl+}**

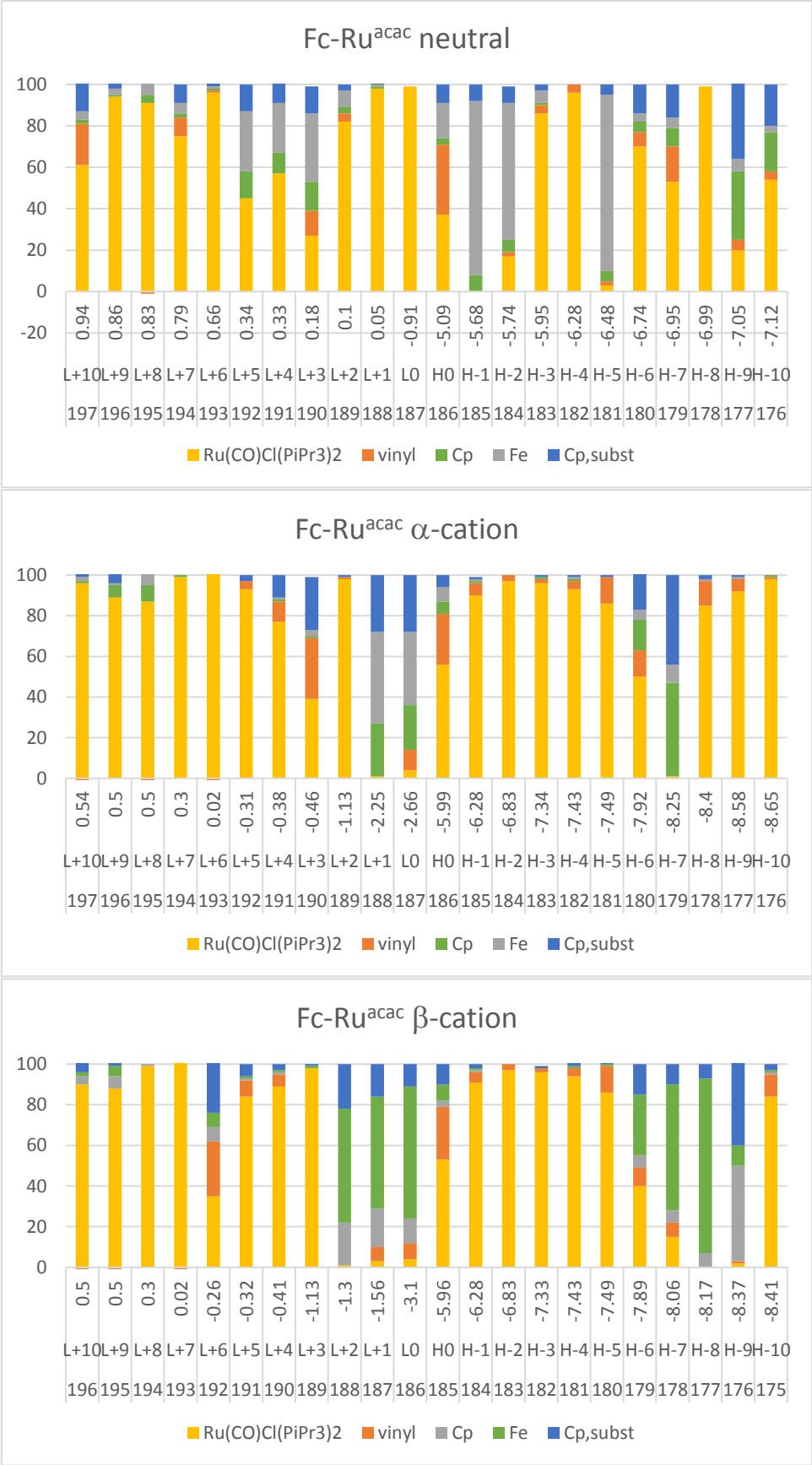

Figure S59: Fragment contributions to the frontier MOs in **Fc-Ru^{acac}** and **Fc-Ru$^{acac\,+}$**

13. Brief Discussion of the Relation between the Shape of an IVCT Band and the Electronic Coupling

MV compounds with electronically coupled redox sites typically exhibit an intervalence charge-transfer (IVCT) band at low energy, usually in the near infrared. Analysis of this band often provides information on the strength of the electronic interaction and the degree of ground state delocalization between the redox sites. In particular, it allows to distinguish between MV systems of Class II[11] with inherently different electron densities and structure parameters at the two conjoined redox sites and strongly coupled MV systems of Class III, where both redox sites are electronically and structurally identical. One criterion is the IVCT band width at half height, $\Delta\tilde{\upsilon}_{1/2}$. According to Mulliken-Hush theory, $\Delta\tilde{\upsilon}_{1/2}$ of a Class II system is larger or equal to the high-temperature limit as defined in equation 1,[12] while $\Delta\tilde{\upsilon}_{1/2}$ for a Class III system is appreciably smaller.[13-15] In equation 1, $\tilde{\upsilon}_{max}$ denotes the energy at the band maximum.

$$\Delta\tilde{\upsilon}_{1/2,theo} = \sqrt{2310\,\tilde{\upsilon}_{max}} \qquad \text{(eq. 1)}$$

$$\Gamma = 1 - \frac{\Delta\tilde{\upsilon}_{1/2,exp}}{\Delta\tilde{\upsilon}_{1/2,theo}} \qquad \text{(eq. 2)}$$

A more refined version of that relation utilizes the parameter Γ defined in equation 2, which is based on the ratio between the experimental and theoretical band widths. Thus, Γ assumes a value of close to zero for valence-localized MV systems of Class I and very weakly coupled MV systems at the Class I/II borderline, of $0 < \Gamma < 0.5$ for MV systems of Class II, of 0.5 for MV systems at the Class II/III borderline, and of >0.5 for Class III systems.[15] Another criterion that can be used to distinguish between MV systems of Class II or III is the extent of solvatochromism of the IVCT band. In the case of a Class II system, the underlying excitation is accompanied by a shift of charge density from the redox site with the higher electron density to the electron-deficient one. A solvent of higher polarity and higher ε_{DK} will stabilize the more polar state and therefore influence the energy of the IVCT band as opposed to a Class III system, where this transition involves hardly any charge-transfer.

14. Solvatochromism of the IVCT Band

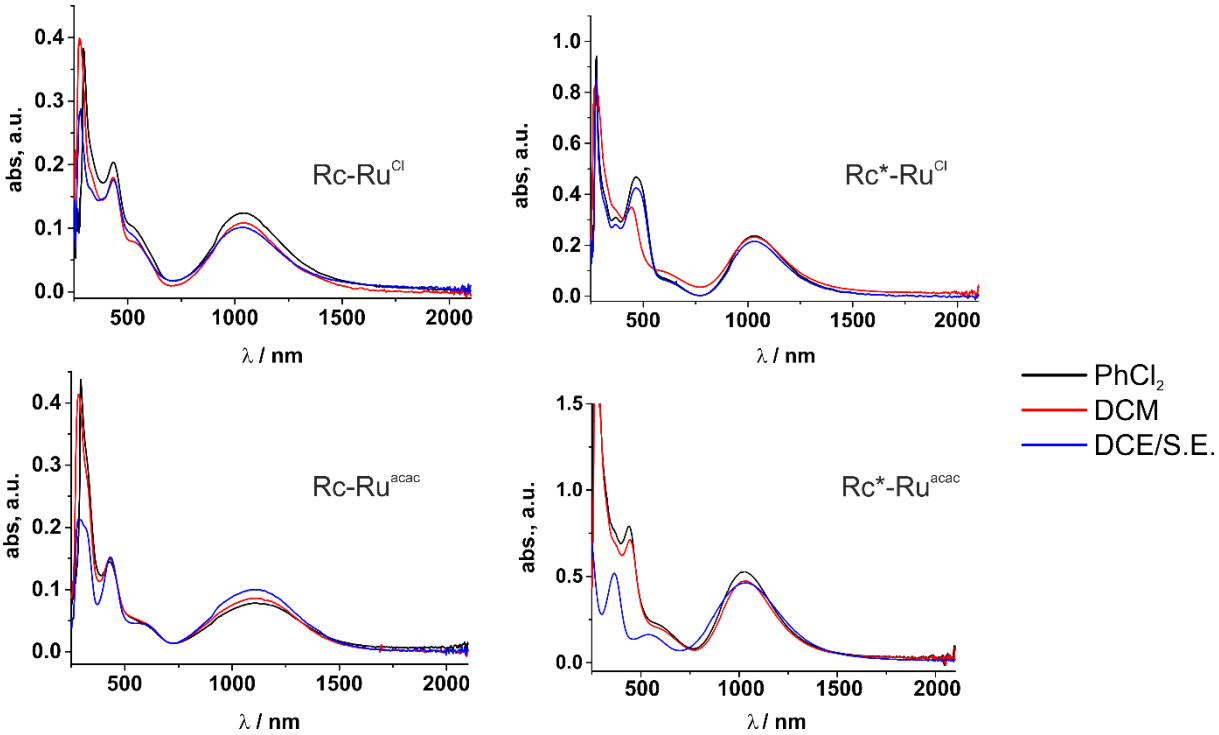

Figure S60: Solvatochromism study of **Rc-Ru^{Cl+}**, **Rc-Ru^{acac+}**, **Rc*-Ru^{Cl+}** and **Rc*-Ru^{acac+}** in *ortho*-dichlorobenzene, dichloromethane and dichloroethane with supporting electrolyte (Bu_4NPF_6).

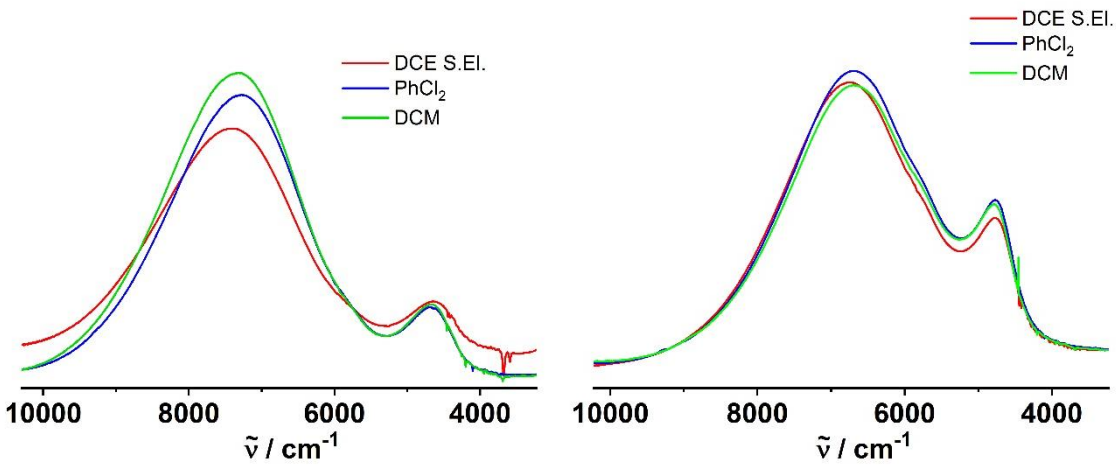

Figure S61: Slight negative solvatochromism found on **Fc-Ru^{Cl}** (left) and **Fc-Ru^{acac}** (right).

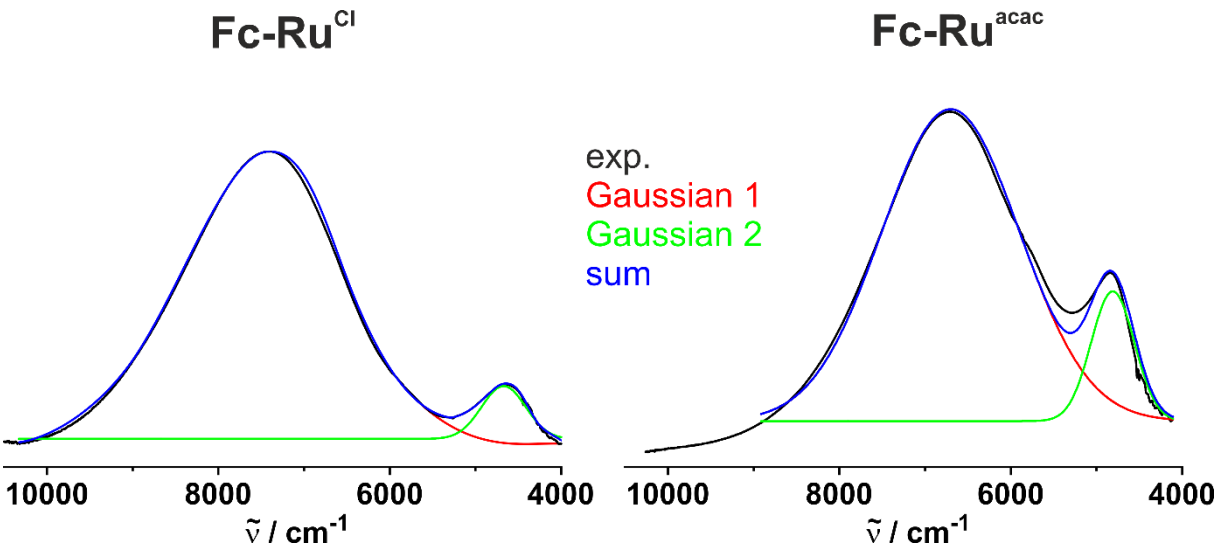

Figure S62: Deconvolution of the NIR bands of the complexes **Fc-Ru^{Cl}** and **Fc-Ru^{acac}** fitted with two Gaussian shaped lines.

15. References

1. Krejcik, M.; Danek, M.; Hartl, F. Simple construction of an infrared optically transparent thin-layer cell: Applications to the redox reactions of ferrocene, $Mn_2(CO)_{10}$ and $Mn(CO)_3$(3,5-di-t-butyl-catecholate)$^-$. *J. Electroanal. Chem.* **1991**, *317*, 179-187.
2. Stoll, S.; Schweiger, A. EasySpin, a comprehensive software package for spectral simulation and analysis in EPR. *J. Magn. Res.* **2006**, *178*, 42-55.
3. Frisch, M. J.; Trucks, G.; Schlegel, H. B.; Scuseria, G. E.; Robb, M. A.; Cheeseman, J. R.; Scalmani, G.; Barone, V.; Mennucci, B.; Petersson, G. A.; Nakatsuji, H.; Caricato, M.; Li, X.; Hratchian, H. P.; Izmaylov, A. F.; Blonio, J.; Zheng, G.; Sonnenberg, J. L.; Hada, M.; Ehara, M.; Toyota, K.; Fukuda, R.; Hasegawa, J.; Ishida, M.; Nakajima, T.; Honda, Y.; Kitao, O.; Nakai, H.; Vreven, T.; Jr., J. A. M.; Peralta, J. E.; Ogliaro, F.; Bearpark, M.; Heyd, J. J.; Brothers, E.; Kudin, K. N.; Staroverov, V. N.; Keith, T.; Kobayashi, R.; Normand, J.; Raghavachari, K.; Rendell, A.; Burant, J. C.; Iyengar, S. S.; Tomasi, J.; Cossi, M.; Rega, N.; Millam, J. M.; Klene, M.; Knox, J. E.; Cross, J. B.; Bakken, V.; Adamo, C.; Jaramillo, J.; Gomperts, R.; Stratmann, R. E.; Yazyev, O.; Austin, A. J.; Cammi, R.; Pomelli, C.; Ochterski, J. W.; Martin, R. L.; Morokuma, K.; Zakrzewski, V. G.; Voth, G. A.; Salvador, P.; Dannenberg, J. J.; Dapprich, S.; Daniels, A. D.; Farkas, Ö.; Foresman, J. B.; Ortiz, J. V.; Cioslowski, J.; Fox, D. J. *Gaussian 09, Revision B.01*, Gaussian Inc., Wallingford, CT, 2010.
4. Andrae, D.; Haeussermann, U.; Dolg, M.; Stoll, H.; Preuss, H. Energy-adjusted ab initio pseudopotentials for the second and third row transition elements. *Theor. Chim. Acta* **1990**, *77*, 123-141.
5. Perdew, J. P.; Burke, K.; Enzerhof, M. Generalized Gradient Approximation Made Simple. *Phys. Rev. Lett.* **1996**, *77*, 3865-3868.
6. Wachters, A. J. H. Gaussian Basis Set for Molecular Wavefunctions Containing Third-Row Atoms. *J. Chem. Phys.* **1970**, *52*, 1033-1036.
7. Cossi, M.; Rega, N.; Scalmani, G.; Barone, V. Energies, structures, and electronic properties of molecules in solution with the C-PCM solvation model. *J. Comput. Chem.* **2003**, *24*, 669-681.
8. Mercier, A.; Yeo, W. C.; Chou, J.; Chaudhuri, P. D.; Bernardinelli, G.; Kündig, E. P. Synthesis of highly enantiomerically enriched planar chiral ruthenium complexes viaPd-catalysed asymmetric hydrogenolysis. *Chem. Commun.* **2009**, 5227-5229.
9. Malachowski, M. R.; Grau, M. F.; Thomas, J. M.; Rheingold, A. L.; Moore, C. E. Heterometallic complexes derived from ruthenocene-functionalized dipyrromethenes. *Inorg. Chim. Acta* **2010**, *364*, 132-137.
10. Sato, M.; Iwai, A.; Watanabe, M. Synthesis and Redox Behavior of Ruthenium(II) 2,3,4,5-Tetramethylruthenocenylacetylide and Related Complexes. Formation of μ-[(Cyclopentadienylidene)-ethylidene]diruthenium Complexes Containing a Strong Metal-Metal Interaction. *Organometallics* **1999**, *18*, 3208-3219.
11. Robin, M. B.; Day, P. Mixed Valence Chemistry - A survey and Classification. *Adv. Inorg. Chem. Radiochem.* **1967**, *10*, 247-422.
12. Hush, N. S. Intervalence Charge Transfer Absorption. Part 2. Theoretical Considerations and Spectroscopic Data. *Prog. Inorg. Chem.* **1967**, *8*, 391-444.
13. Sutin, N. Nuclear, electronic, and frequency factors in electron transfer reactions. *Acc. Chem. Res.* **1982**, *15*, 275-282.
14. Sutin, N. Theory of electron transfer reactions: insights and hindsights. *Prog. Inorg. Chem.* **1983**, *30*, 441-498.
15. Brunschwig, B.; Creutz, C.; Sutin, N. Optical transitions of symmetrical mixed-valence systems in the Class II-III transition regime. *Chem. Soc. Rev.* **2002**, *31*, 168-184.